Chapter 6
Multiscale Modeling Examples: New Polyelectrolyte Nanocomposite Membranes for Perspective Fuel Cells and Flow Batteries

Soumyadipta Sengupta, Alexey V. Lyulin, Georgios Kritikos, Konstantinos Karatasos, Arun Venkatnathan, Rakesh Pant, and Pavel V. Komarov

Abstract Renewable energy production from fuel cells and energy storage in flow batteries are becoming increasingly important in the modern energy transition. Both batteries use polyelectrolyte membranes (PEMs) to allow proton transport. In this chapter, both PEMs and PEMs-based nanocomposites have been discussed using various simulational approaches. A coarse-grained model of a Nafion film capped by the substrates with variable wettability has been used to simulate nanocomposites

S. Sengupta · A. V. Lyulin (✉)
Group Theory of Polymers and Soft Matter and Center for Computational Energy Research, Department of Applied Physics, Technische Universiteit Eindhoven, 5600 MB Eindhoven, The Netherlands
e-mail: a.v.lyulin@tue.nl

S. Sengupta
e-mail: s.sengupta@tue.nl

G. Kritikos · K. Karatasos
Department of Chemical Engineering, Aristotle University of Thessaloniki, 54124 Thessaloniki, Greece
e-mail: kritikgio@gmail.com

K. Karatasos
e-mail: kkaratas@cheng.auth.gr

A. Venkatnathan · R. Pant
Department of Chemistry and Center for Energy Science, Indian Institute of Science Education and Research, Dr. Homi Bhabha Road, Pashan, Pune, Maharashtra 411008, India
e-mail: arun@iiserpune.ac.in

R. Pant
e-mail: rakesh.pant@students.iiserpune.ac.in

P. V. Komarov
A.N. Nesmeyanov Institute of Organoelement Compounds of Russian Academy of Sciences, Vavilova st. 28, 11999 Moscow, Russia
e-mail: pvkomarov@gmail.com

Tver State University, Sadoviy per. 35, 170002 Tver, Russia

of PEMs by classical molecular-dynamics (MD) method. Classical MD modeling results have also been reviewed for a PEM-graphene oxide nanocomposite internal structure and dynamics. Ab-initio simulations have been implemented to describe the proton transfer pathways in anhydrous PEMs. Finally, the large-scale mesoscopic simulations have been introduced to shed light on the water domain features present in the hydrated PEMs. A brief description of polybenzimidazole membrane as electrolyte and Ionic Liquids as dopants for fuel cells is also presented.

6.1 Introduction

In this chapter, the application of the multiscale modeling methods has been discussed for a very special class of the nanocomposites—polymer electrolyte membranes (PEMs), one of the key elements of the modern fuel cells [1, 2] and flow batteries [3]. Low-temperature fuel cells (FCs) based on polymer ion-exchange membranes powered by hydrogen or methanol are often considered as a replacement for traditional power sources in motor transport and household devices [1]. Their main advantages are portability, low operating temperature (<100 °C), and simplicity of the internal design.

The fuel cell design is quite simple, see Fig. 6.1. It consists of two electrodes and a solid electrolyte. The following types of FC are distinguished: alkaline, carbonate, solid oxide, with a polymeric proton-exchange membrane and phosphoric acid. With respect to operating temperature, the FCs are divided into low-temperature FC (operating temperature <100 °C), medium-temperature FC (<220 °C), and high-temperature FC (600–1000 °C).

In the low-temperature hydrogen fuel cells, the role of electrolyte is played by an ion-exchange membrane. In general, PEM represents a thin film of a polymer with ionogenic groups. The role of membrane is to separate the flow of fuel from
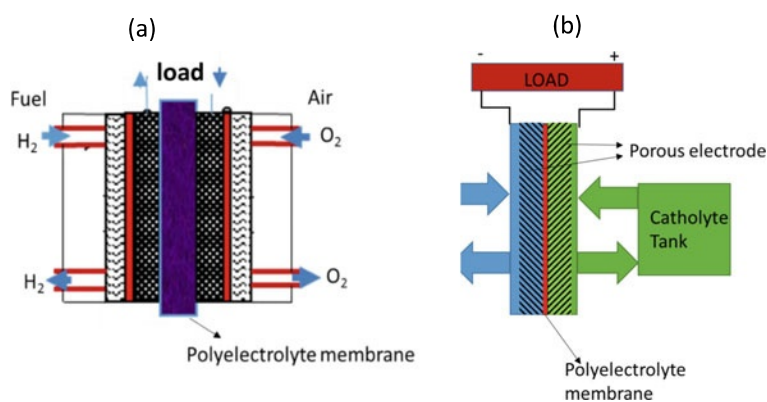

Fig. 6.1 Schematics of the **a** a hydrogen–oxygen fuel cell and **b** a redox flow battery

the oxidizer and to serve as an electron insulator. Hydrogen molecules are oxidized at the anode ($H_2 \rightarrow 2H^+ + 2e^-$) and the formed protons are transferred to the cathode through the membrane [1]. The released electrons pass through an external circuit and are transmitted to the cathode, creating electric current. At the cathode block, in the presence of the catalyst, the reaction $O_2 + 4e^- \rightarrow 2O^{2-}$ occurs. The cycle of the recombination electrochemical transformations is completed with the reaction of oxygen ions with protons; as a result, the water molecules are formed, $O^{2-} + 2H^+ \rightarrow H_2O$. The theoretical value of the electromotive force (EMF) of a hydrogen–oxygen FC at 25 °C is 1.23 V; the no-load voltage is about 1 V. Such FCs have the lowest operating temperature of 40–80 °C, which is both their advantage and disadvantage. The simple design of the low-temperature FCs allows them to be made compact, but, unfortunately, at these temperatures, the platinum catalyst is very sensitive to the degree of the fuel contamination. Therefore, research aimed to improve the efficiency of such FCs is performed in two directions: the development of the highly efficient membranes and the search for chemically resistant and cheap catalysts.

It is assumed that for use in FCs, the membrane conductivity should be above 0.001 S/cm [1–3]. Since PEMs perform the functions of a gas separator and an electrical insulator, it is necessary that these membranes possess low gas permeability and electrical conductivity. In addition, they should have sufficient mechanical strength. This is required for operation at high pressures. Furthermore, the membrane should not be destroyed as a result of electrodes pressing on. Since during the electrochemical reactions peroxide compounds, such as H_2O_2, OH^-, and HOO^- can be formed, the membranes should demonstrate high chemical resistance to oxidation and hydrolysis [1–3].

PEMs are also used in redox flow batteries (RFB) as shown in Fig. 6.1b. The catholyte and the anolyte form a redox couple in which the anolyte gets oxidized and releases electron into the external circuit. The electron travels through the external circuit and reaches the cathodic side to reduce the catholyte. There also exist some protons released during this process which travel toward the cathodic side to maintain the charge balance in the system; the PEM helps in transport of these protons. The speed of charging and discharging is affected by the ease of proton transport across the PEM. The PEM also prevents the catholyte and the anolyte from crossing over and mixing. Such mixing would reduce the efficiency of the battery and could also lead to catastrophic power discharge and fire.

When water is added to the PEM, the microphase separation of the hydrophilic and hydrophobic segments of the polymer chains occurs. It leads to the formation of water domains localized near the hydrophilic groups. As a result, various hydrated proton complexes, i.e., hydronium ions (H_3O^+), Zundel ($H_5O_2^+$) and Eigen ($H_9O_4^+$) cations are formed. With the increasing amount of water, the water domains merge into a continuous network of water channels that provide proton transport through the membrane volume as shown in Fig. 6.2. At the same time, the hydrophobic domains enhance the mechanical strength of the membranes. They are formed from the fluorinated, aromatic or aliphatic segments of macromolecules. The sulfonic acid groups ($-SO_3H$) and the phosphate groups ($-PO_3H_2$) are the most commonly used
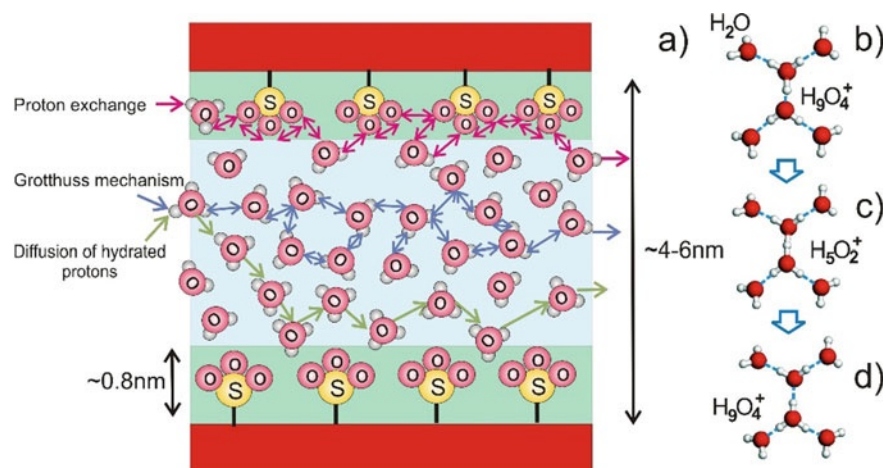
Fig. 6.2 The mechanisms of proton transport: **a** in the ion channel, **b–d** the stages of proton transfer
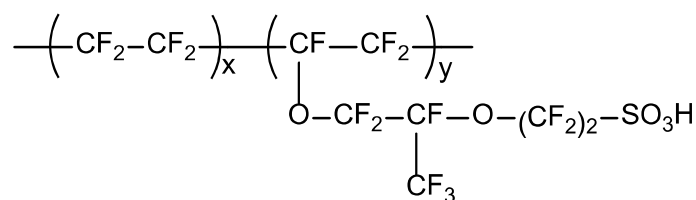

Fig. 6.3 The general structural formula of the Nafion® family polymers

ionic acid-type groups, dissociating with the release of a proton. Sulfonated polymers are more efficient at high degree of hydration, while phosphorylated polymers can function with a low water content and have high heat resistance.

Conventionally, the Nafion derivatives (see Fig. 6.3) are the copolymers of tetrafluoroethylene and perfluorinated vinyl ether side chains with sulfonic acid groups at ends. Membranes based on such polymers are durable, resistant to oxidation and have a record high ionic conductivity (up to 0.1 S/cm at temperatures below 80 °C). The disadvantages of Nafion are the narrow range of the operating temperatures (<90 °C). Limitation of the temperature range leads to the need for utilization of highly purified hydrogen, since even small CO impurities impart a destructive effect on the platinum catalyst. Increasing the operating temperature to above 120 °C allows to shift the equilibrium of the CO and H_2 sorption on the catalyst toward hydrogen. This prevents the poisoning of the catalyst, but it is impossible to raise the temperature above 90 °C. Upon increasing temperature, the water content in the ion channels decreases due to water evaporation. This causes the diameter of the water channels to narrow. If the water content is below the percolation threshold, the network of water

channels is disrupted. It is accompanied by a sharp drop in the membrane conductivity. The ionic conductivity of the dry polymer is not sufficient for the operation of FC. The efficient transfer of protons can be ensured only if constant hydrostatic level is maintained. This requires introducing additional structural elements and increases the total cost of the batteries.

In [4, 5] the modification of Nafion by silicon dioxide nanofillers has been studied. Such nanocomposites demonstrate the ability to function effectively at temperatures up to 140 °C, as their ability to retain water at high temperatures increases. In addition to the studies on the modifications of Nafion, research is actively conducted to find alternative solid polyelectrolytes based on mass-produced polymers with an aryl skeleton, such as polycarbonates, polyesters, polystyrenes, and polysulfonic acids [6]. Membranes based on polybenzimidazole (PBI) modified with phosphate groups possess high thermal stability and conductivity in dry conditions. Their operating temperature range is 160–180 °C, which allows their use in medium-temperature FCs. However, upon contact with water, the acid–base complex is destroyed, and the phosphoric acid is washed out into catalytic and gas-diffusion layers. This leads to the blockage of the gas pores, degradation of the electrodes and of the whole gas pipeline system. At the same time, the proton conductivity of the membrane decreases sharply. Another relatively simple method to obtain ion-exchange membranes can be implemented by modifying the polymer matrix with side chains followed by sulfonic acids [7]. This method to obtain ionomers requires lower costs than when using Nafion. The proton conductivity in this case is 0.11 S/cm at 100% hydration and $T = 298$ K. The main disadvantage of such membranes is a high degree of swelling, greatly exceeding similar values for Nafion. There have been also attempts to obtain high-performance membranes based on polysulfonic acids, polyethersulfonic acids, polyimides, and sulfonated poly(ether-ether ketone) (SPEEK) [8–14].

The exact mechanism of the PEM protons transfer is the highly debated subject; the proton transport is described in some detail by Agmon [15]. Two possible mechanisms of the proton transfer through the membrane are discussed. Sulfonic acid groups, which are concentrated mainly on the walls of the channels, dissociate in the presence of water to form ion pairs: $-SO_3H + H_2O \rightarrow -SO_3^- + H_3O^+$. According to the classical Grotthuss mechanism, the protons are transferred through a continuous proton-exchange reaction: $H_2O + H^+ \leftrightarrow H_3O^+$, see Fig. 6.2a. Other mechanisms suggest the protons transfer as a result of the hydronium ions diffusion and hops between adjacent sulfonic acid groups [16]. In this case, the rate of proton exchange depends on the difference in the probabilities of proton capture by water molecules and by sulfonic acid groups.

Figure 6.2b shows the hydronium ion H_3O^+, surrounded by solvated water molecules, forming the Eigen–cation $H_9O_4^+$ [17]. It is hydrated as well, but the hydrogen bonds in the second coordination sphere of H_3O^+ are weaker than in the first sphere. It is assumed that the proton exchange is initiated by a random change in one of the hydrogen bonds between the water molecules forming the second coordination sphere of hydronium. This causes a rapid change in the orientation of water molecules (over a time of the order of 1 ps), which can lead to the breaking of one of the hydrogen bonds. In the remaining cluster, a quick rearrangement of the bond

lengths and angles occurs forming a complex $H_2O \cdots H^+ \cdots H_2O$ Zundel cation ($H_5O_2^+$) [18] as shown in Fig. 6.2c. In this complex, in turn, as a result of fluctuations in the bond lengths, the proton can join one of the two water molecules forming a new hydronium ion as shown in Fig. 6.3d. Next, the hydration shell is formed, and the process repeats.

Ab-initio molecular-dynamics (MD) calculations [19–21] confirm that proton transfer is realized through a continuous chain of transformations of Eigen and Zundel cationic complexes. In the empirical valence bonds model, using the example system of a small Nafion/water system (~5000 atoms and 40 excess protons), a detailed study of the Grotthuss mechanism was performed [22, 23]. This model allows the hopping movement of protons from hydronium ions to the nearest water molecules. In a hybrid model using the classical and the quantum–mechanical methods [24], the proton migration was studied for a system containing a single Nafion oligomeric chain with 10 SO_3^- groups, the same number of H_3O^+ ions and 156 water molecules. In [21], using extensive 120-ps-long density-functional theory (DFT)-based simulations of charge migration in the 1200-atom model of the hydrophilic Nafion nanochannel, a bimodality of the van Hove autocorrelation function $G_s(\mathbf{r}, t)$ has been observed. This provides direct evidence for the Grotthuss hopping mechanism being a significant contributor to the proton conductivity.

The PEM proton conductivity strongly depends on the water content in the membrane. The amount of water in the membrane is often characterized by the volume fraction φ and the hydration parameter λ (the number of water molecules per sulfonic acid group). Nafion becomes a proton conductor at $\lambda \approx 2–5$ [21, 25]. In this case, the fraction of hydrated sulfonic acid groups is very small, and they should exist only within segmental clusters.

Hydrophilic membrane domains containing $–SO_3H$ groups have a high affinity to water. Even after air drying, the proton of the sulfonic acid group continues to bind two water molecules. Upon contact with water, the degree of the membrane hydration increases dramatically due to the absorption of water [26–29], which leads to the membrane swelling and to an extensive reformation of its structure.

The presence of well-defined maxima in the intensity of small-angle X-ray scattering (SAXS) data for sulfonic acid membranes shows that their structure must contain ordered water clusters [29, 30]. Based on the analysis of experimental data, Gierke proposed some generalized model of the structure of perfluorinated sulfonic acid membranes [28, 31] as shown in Fig. 6.4. According to this model, the membrane consists of an array of linked clusters connected by narrow channels. On the periphery of the clusters, which in a first approximation have a spherical shape, sulfonic acid groups are located. As a result, the surface energy is minimized and the contact of the hydrophobic segments of the matrix chains with water is limited. The internal volume of the cluster is filled with water molecules and its proton complexes, which are formed during the dissociation of the functional groups. The migration of the proton complexes occurs from cluster to cluster via the extensive network of channels, which can break off with low moisture content. If this happens, the membrane loses its transport properties. Even though this model is widely used, other possible variants of the membrane structure, which also allow the description of the SAXS
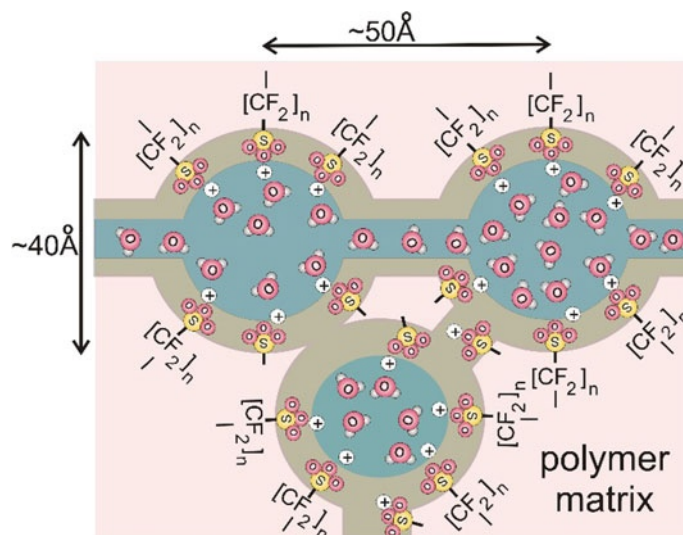
Fig. 6.4 The cluster-channel model of Nafion, proposed by Gierke [28]

results, are present in the literature. One could mention here Fujimura's modified core–shell model [32, 33], Dreyfus's local ordering model [34], Litt's lamellar model [35], and Rubat's rod-like aggregates model [36]. A common feature of these models is adoption of the fact that sulfonic acid groups in a hydrophobic matrix form a penetrating network of linked ionic clusters that swell in a polar solvent and provide ion transport of the membrane. At the same time, each of the models provides its description of the topology of the structure of the ion channels network. In addition to these models, Schmidt–Rohr and Chen [37] proposed parallel cylindrical channels inside a hydrated Nafion membrane. These channels were lined-up with sulfonic acid groups and were filled with water and protons.

Based on the results of X-ray and neutron scattering experiments on samples of Nafion membranes with different water contents, as well as on the basis of energy considerations, Gebel [26] proposed a concept to describe the process of swelling and dissolving ionomers. It is assumed that the dry membrane contains separate isolated ion clusters with a diameter of about 1.5 nm. They swell when water enters the membrane. When the water content in the membrane reaches a percolation threshold λ^*, a linked network of the water clusters forms in the membrane, and the membrane becomes a conductor of ions. With further absorption of water, an inversion of the structure occurs, and, as a result, the system structure takes the form of a network of intertwined rods. A further increase in the water content leads to the complete dissolution of the membrane with the formation of a colloidal dispersion of individual rod-like fibers.

PEMs which require humidification for proton conduction limit the deployment of fuel cells with operating temperatures up to the boiling point of water. The operation of these fuel cells at higher temperature reduces catalyst poisoning, and

hence, suitable alternatives as proton carriers have been explored [38, 39]. Aromatic membranes such as Poly (2,5-benzimidazole) (ABPBI), Poly[2,2-(m-phenylene)-5,5-bibenzimidazole) doped with phosphoric acid (PA) have been explored for high-temperature fuel cells. These membranes have excellent properties such as high thermal, chemical and mechanical stability, high conductivity at elevated temperatures and low cost [40, 41]. ABPBI membrane has nitrogen (N) atom on the imidazole ring which serves as a proton acceptor [42] and can interact with dopants. ABPBI shows higher affinity toward PA as compared to PBI, due to the absence of phenyl ring. PA is amphoteric and has a high boiling point, which makes it a suitable proton conductor for fuel cell applications [41]. PBI membrane has high glass-transition temperature (430 °C), excellent chemical resistance, and mechanical strength which stems from the aromatic backbone. The PA-doped PBI has high proton conductivity (0.07 S/cm) in fully doped conditions and is comparable to the state-of-the-art PFSA membranes. In PBI, high conductivity extends up to 200 °C. IR [40, 43, 44], Raman [45], and NMR spectra [46] have confirmed the presence of strong hydrogen bonds between PA and the nitrogen atom on the imidazole, resulting in the formation of $H_2PO_4^-$.

Ionic liquids (ILs) are considered as a promising alternative to water due to their excellent properties such as high thermal stability, low vapor pressure, wide electrochemical window, and high anhydrous ionic conductivity. These properties render ILs promising dopants in electrolytic membranes, and, thus, enabling operation of PEMFC at higher operating temperatures (>100 °C). A protic ionic liquid (PIL) is defined as a combination of a Brønsted base and Brønsted acid, where the base accepts a proton from the acid [47]). The use of PILs as proton carriers has been explored for high-temperature fuel cells [47–49]. A wide range of PILs as a prospective proton conducting material and underlying proton conduction mechanism has been investigated with excess of one constituent, or in PIL-doped membranes [47, 50–54]. Sood et al. [53] demonstrated that IL (triethylammmonium trifluorosulfonate, TFTEA) doping in Nafion (neutralized with triethylamine, TEA) enhances the ionic conductivity anhydrous conditions. The conductivity of IL-doped membrane increases with wt% of IL.

In the next parts of this chapter, computer simulations of some of these PEMs and their nanocomposites are discussed in more detail.

6.2 Multiscale Modeling of Polyelectrolyte Membranes and Their Transport Properties

By now, many theoretical studies on the properties of Nafion have been published [21, 55–57]. However, the studies of other ion-exchange polymers, in particular, sulfonated polyheteroarylenes, are practically absent. Although Nafion and polyheteroarylenes differ significantly in their chemical structure, the formation of the

structure of sulfonated polymers must follow general principles. Therefore, the analysis of the accumulated results about Nafion can be useful in the study of other sulfonated acid polymers.

The earliest studies were carried out in the framework of semi-empirical methods with a large number of parameters, adjusted according to experimental data [36, 58–60]. They drew general conclusions regarding the origins of the microphase separation in ionomers into hydrophilic and hydrophobic domains, but they did not provide a detailed description of the membrane structure.

The next group of theoretical approaches includes methods based on atomistic simulations [61–68]. They allow to simulate the microphase separation of polar and non-polar segments of polymer chains and to study the diffusion of water and hydronium. This helps to understand how the local ordering occurs in PEMs, depending on the water content and on the role of the side chains of fluoropolymers containing sulfonic acid groups.

The most rigorous level of consideration was achieved using the quantum–mechanical methods [19, 20, 69–71]; accurate data have been obtained on the properties of different molecular groups, the dissociation of $-SO_3H$, the conformations of fragments of the Nafion chain, and the mechanism of the proton transport.

The experimental and theoretical studies of ion-exchange membranes show that in order to explain the structural features of the water channels of proton-conducting membranes, it is necessary to consider the morphology of ionomers on spatial and temporal scales that significantly exceed the capabilities of atomistic methods. In this case, mesoscopic approaches, such as cellular automaton method [72], MC/PRISM (a combination of Monte Carlo methods and integral equations) [73], the dissipative particle dynamics (DPD) method [74, 75], and a dynamic version of the density-functional theory method (DDFT) [76, 77], can provide the most detailed information. The predictions obtained in the framework of the aforementioned approaches are in a good agreement with pertinent experimental results and with findings from the atomistic modeling. However, neither DPD nor DDFT is suitable for studying the mechanisms of ion transfer.

As has been mentioned before, the Nafion-based nanocomposites fabricated by mixing with nanoparticles are often used in fuel cells and flow batteries to improve proton conductivity, water retention levels and selectivity to the motion of protons only. Classical MD simulation studies of such nanocomposites are appropriate to understand the internal water cluster structure and transport characteristics. Nafion nanocomposites containing highly hydrophilic nanoparticles, like modified silica, have exhibited higher proton conductivity as compared to that of bulk Nafion [78]. Methanol crossover in direct methanol fuel cells and vanadium crossover in flow batteries have been reduced by using such Nafion nanocomposites [79, 80]. In [80], the reduction of methanol crossover and increased proton conduction in a Nafion-modified carbon nanotube (CNT) nanocomposite has been observed. It was proposed that such effects were due to the formation of long hydrophilic pathways along the modified CNTs. All these experiments point toward the need for a better understanding of Nafion–nanoparticle interfaces.

Nafion nanocomposites show a large variation in nanoparticle sizes (5–75 nm) [81, 82]. Therefore, Nafion–nanoparticle interface could be modeled using a coarse-grained description of a Nafion film-flat substrate interface with lateral dimensions in the range of 4–6 nm. Nanocomposites may possess different filler densities which affect the average interparticle distances. The average interparticle distance in a Nafion/titania nanocomposite was found to be 9 nm [81]. Also, previous experiments have sought a more thorough understanding of the structure in Nafion films of thickness less than 10 nm, because this is exactly the range of the interparticle distances commonly met in catalyst layers [83]. Therefore, film thicknesses in the range of 6–11 nm can be chosen to perform the classical coarse-grained MD simulations.

Different types of nanoparticles like silica, zirconia, and modified carbon nanotubes [78, 81] with varying wettabilities have been used in Nafion nanocomposites. In addition, Nafion also exists in catalyst layers between carbon support and platinum nanoparticles [82, 84].

In the next paragraph, a hydrated Nafion film capped by substrates of varying hydrophilicity will be discussed in some detail. Such a model, introduced in [78] initially for the elastomer-based nanocomposites, has been recently used to provide useful insights into the interfacial interactions in Nafion nanocomposites.

6.3   Confined Film Model of a Nanocomposite Membrane

Classical molecular-dynamics (MD) techniques were used for thr simulations. A polymer nanocomposite is comprised by fillers/nanoparticles dispersed inside the polymer matrix as shown in Fig. 6.5a. The representative volume element (RVE) modeled in the simulations is the polymer material present between any two nanoparticles as a confined film. This RVE was modeled by confining 17 Nafion chains along with water molecules and hydronium ions between structureless walls of tuneable hydrophilicity [85, 86] as shown in Fig. 6.5b. A fixed moderate hydration level of λ = 15 was used for the simulations. The walls represent the nanoparticle surfaces of variable hydrophilicity.

An integrated Lennard–Jones potential [87],

$$E = \epsilon \left(\frac{2}{15} (\sigma/r)^9 - (\sigma/r)^3 \right), r < r_c \tag{6.1}$$

has been used to simulate structureless walls at the top and at the bottom of the simulation box [85]. In (6.1) r_c is the cut-off radius, and the interaction energy ϵ of the walls with the hydrophobic parts of the system (i.e., the Nafion molecule except the sulfonic acid groups) was $\varepsilon_{phob} = 0.25$ kcal/mol. Five different values of interaction energy ε_{phyl} of the walls with the hydrophilic part of the system were used in the simulations. Henceforth, walls with $\varepsilon_{phyl} = 0.25, 0.50$ kcal/mol will be referred to as low hydrophilicity (LH) walls and those with $\varepsilon_{phyl} = 1.20, 1.50, 2.00$ kcal/mol will be referred to as high hydrophilicity (HH) walls. In both cases, ϵ_{phob} has been
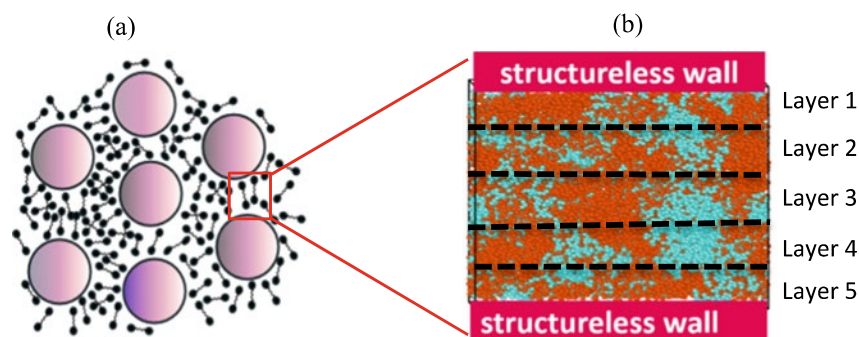
Fig. 6.5 **a** A schematic representation of a nanocomposite membrane. The spheres are the nanoparticles while the black bead-springs are the hydrated Nafion. The hydrated Nafion volume bound between two nanoparticles as shown by the red square is the representative volume element (RVE). This RVE is modeled as a capped film as shown in **b** hydrated Nafion film is capped by two structureless walls. Z-axis is the direction perpendicular to the walls and *X*- and *Y*-axes are parallel to the walls. Z-direction has fixed boundaries and the film is periodic in *X*- and *Y*-directions. Blue color represents water molecules and hydronium ions; orange color is used for Nafion molecules. Water transport is analyzed in the five different layers of the film [66]

fixed at 0.25 kcal/mol [66, 85, 86]. Three different film thicknesses of 6.3, 8.7, and 11.5 nm were simulated for each of the ε_{phyl} values. The film thickness was varied in the Z-direction (Fig. 6.5b). The thickness variation modeled the variation of the filler fraction in a nanocomposite, i.e., higher film thickness corresponded to lower filler fraction and vice versa.

Figure 6.6 shows the simulated Nafion film snapshots at the end of the production runs for five different values of wall hydrophilicity. For low values of wall hydrophilicity ($\varepsilon_{phyl} = 0.25, 0.50$ kcal/mol), there is very little accumulation of water molecules near the walls. However, for the high hydrophilicity walls ($\varepsilon_{phyl} = 1.20, 1.50, 2.00$ kcal/mol), a noticeable accumulation of water near the walls is observed.

Due to sufficiently high hydration levels, water channels in Nafion form a percolated network [24] which facilitates a proton transport. However, such a percolated network can also allow unwanted crossover of methanol and vanadium ions. Nafion nanocomposites have been shown to reduce the crossover of methanol [80] and vanadium ions [88]. Therefore, water cluster analysis was usually done for the different values of wall hydrophilicity. All the water cluster analysis shown here is for a cut-off distance of 3.7 Å averaged over 3 ns of the simulated physical time [66].

Water cluster distribution at a fixed film thickness and different values of wall hydrophilicity is shown in Fig. 6.7. The cluster distributions for the LH walls ($\varepsilon_{phyl} = 0.25, 0.50$ kcal/mol) are almost the same as that of the bulk hydrated Nafion ($\lambda = 15$) cluster distribution. The large clusters (cluster size close to 2400) for the HH walls ($\varepsilon_{phyl} = 1.20, 1.50, 2.00$ kcal/mol) occur less frequently as compared to the LH walls. In addition, there is an emergence of clusters in the 900–1500 size range for the HH walls. This shows that the cluster sizes reduced considerably with increasing
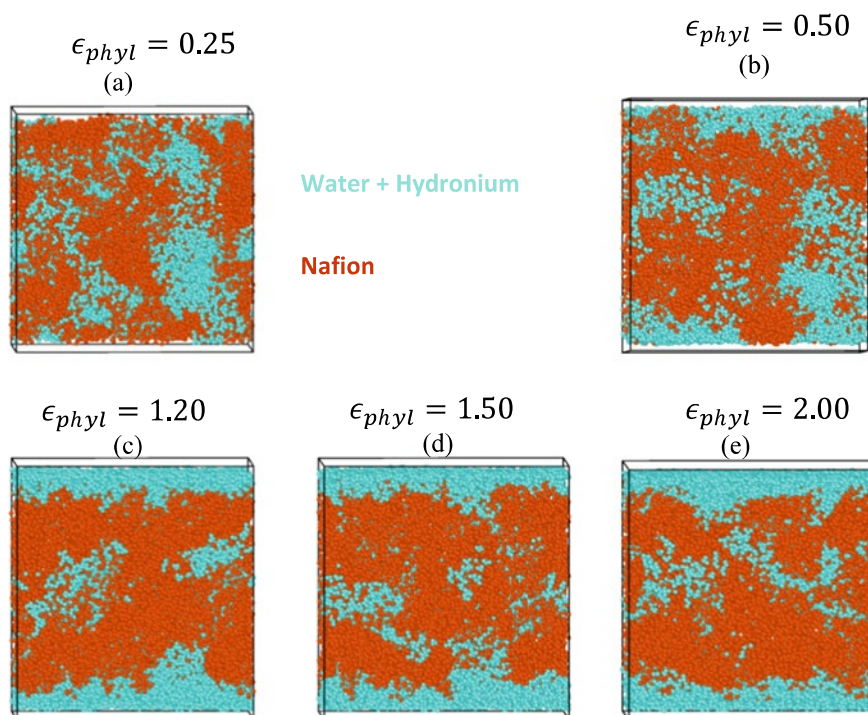
$\epsilon_{phyl} = 0.25$
(a)

Water + Hydronium

Nafion

$\epsilon_{phyl} = 1.20$
(c)

$\epsilon_{phyl} = 0.50$
(b)

$\epsilon_{phyl} = 1.50$
(d)

$\epsilon_{phyl} = 2.00$
(e)

Fig. 6.6 Snapshots for **a** $\varepsilon_{phyl} = 0.25$ kcal/mol **b** $\varepsilon_{phyl} = 0.50$ kcal/mol **c** $\varepsilon_{phyl} = 1.20$ kcal/mol **d** $\varepsilon_{phyl} = 1.50$ kcal/mol **e** $\varepsilon_{phyl} = 2.00$ kcal/mol where blue color shows the water molecules and hydronium ions, and orange color shows the Nafion atoms. Reprinted with permission from [66]. © 2018 American Chemical Society

hydrophilicity of the walls for a fixed film thickness of 6.3 nm. Similar effects are also seen for larger films thickness.

Figure 6.8 shows the water cluster count normalized by the bulk Nafion ($\lambda = 15$) water cluster count, for different wall hydrophilicities and film thicknesses. All the normalized cluster counts are larger than 1, meaning that the number of water clusters for all the wall hydrophilicity values and the film thicknesses were greater than that of bulk hydrated samples. This implies a more dispersed water cluster network in the Nafion films, as compared to the bulk hydrated Nafion.

The water cluster count increases for the HH walls as compared to the LH walls for all three different film thickness values as shown in Fig. 6.8. This effect is universal and is weakly dependent on the film thickness. The higher cluster count indicates a more dispersed water cluster network for the HH wall films as compared to the LH wall films, which can also be seen in the inset for the HH wall films as shown in Fig. 6.7. Relevant experiments have shown that unwanted crossover reduces due to the highly hydrophilic nanoparticles like silica, clay, etc. [79] added to Nafion. In fact, the existence of the long-range-oriented pathways along the modified carbon
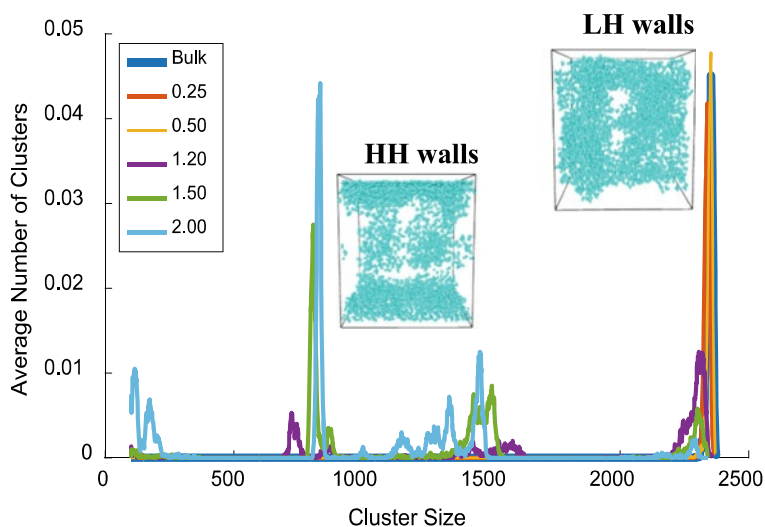
Fig. 6.7 Water cluster distribution for the 6.3 nm film at different wall hydrophilicity values, also for bulk Nafion. The cluster distribution shown is for the cluster sizes ranging from 100 to 2380 water molecules. Reprinted with permission from [66]. © 2018 American Chemical Society
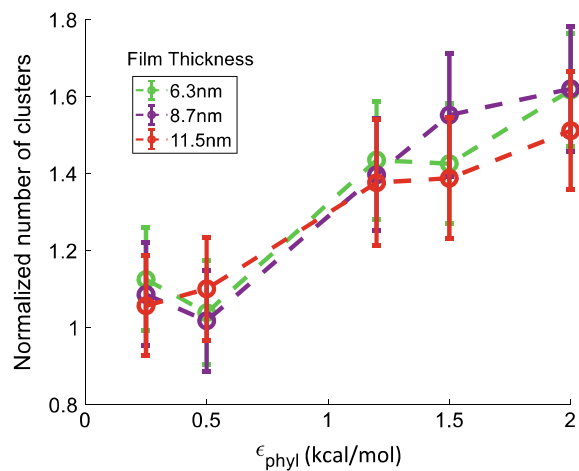

Fig. 6.8 Dependence of water cluster count, normalized by the bulk cluster count, as a function of different wall hydrophilicity (ϵ_{phyl}) for different film thickness [66]

nanotubes was the proposed mechanism for the observed enhanced proton transport and reduced methanol crossover in a Nafion—modified CNT nanocomposite [80]. The MD simulations [66] also show the preferential accumulation of water along the HH walls and a concomitant increase in the water cluster count due to the emergence of a more dispersed water phase and isolated water clusters. It is likely that less polar
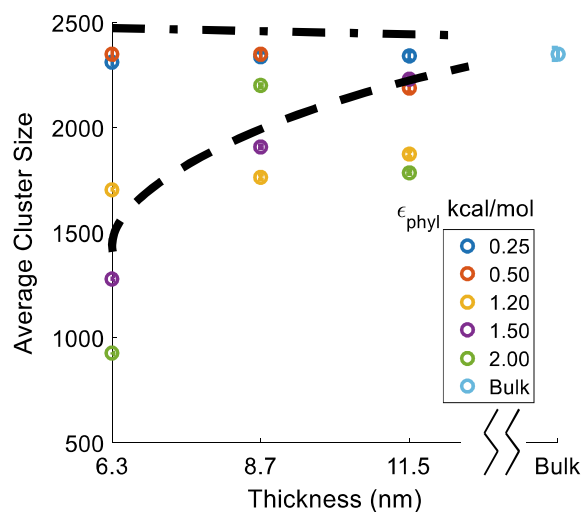
Fig. 6.9 Average water cluster size versus different film thickness for different wall hydrophilicity (ϵ_{phyl}). Average cluster size for bulk Nafion is also shown. The dash-dot line shows the trend for the low hydrophilicity walls and the dash line shows the trend for the high hydrophilicity walls. These lines are not numerical fits. Reprinted with permission from [66]. © 2018 American Chemical Society

molecules, like methanol, will move away from the highly hydrophilic nanoparticles, similar to carbon moving away from the HH walls, as shown in Fig. 6.6. This will increase the chances of such molecules being trapped in the isolated clusters which are found at larger distances from the HH walls as seen in the inset of Fig. 6.7.

Figure 6.9 shows the average water cluster size for different wall hydrophilic-ities and film thicknesses. For the LH walls, the average cluster sizes remain almost constant upon increasing the film thickness. However, the average water cluster sizes show an increasing trend with increasing film thickness for the HH walls. This trend for the HH walls indicates higher phase separation between the water/hydrophilic phase and the hydrophobic phase with increasing film thick-ness, leading to larger average water cluster sizes. Previous transmission electron microscopy (TEM) images [83] and GISAXS experiments [89] have shown similar trends in the water/hydrophilic phase domain sizes vs film thickness for Nafion films supported on hydrophilic silica substrates.

Water diffusion plays a key role in the performance of Nafion. The proton attaches itself to the water molecules and diffuses in the membrane. Therefore, water diffusion constants (D_x, D_y and D_z) have been computed in [66] for the X-, Y-, and Z-directions using the Einstein relation for diffusive motion. Water diffusion in the films' XY-plane is studied using the in-plane diffusivity (D),
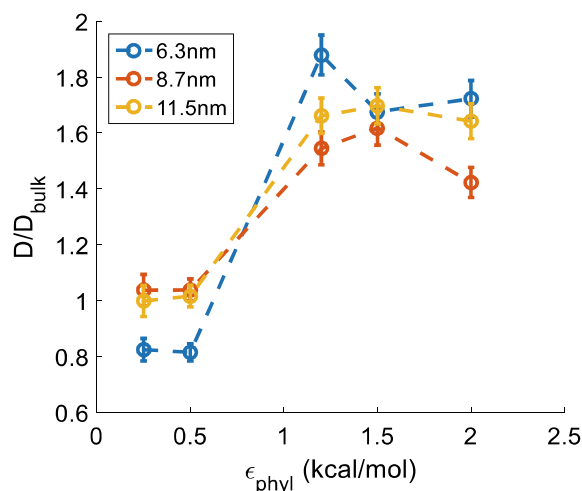
$$D = (D_x + D_y), \tag{6.2}$$

Fig. 6.10 Film averaged in-plane water diffusion constants (D) normalized by the corresponding two-dimensional water diffusion (D_{bulk}) constant at $\lambda = 15$ for bulk Nafion. Reprinted with permission from [66]. © 2018 American Chemical Society

and was compared to the analogous (two-third of the total water diffusion coefficient) values for hydrated Nafion bulk (D_{bulk}),

$$D_{bulk} = \left(\frac{2}{3}\right) * (D_{bulk-x} + D_{bulk-y} + D_{bulk-z}) \tag{6.3}$$

Henceforth, the diffusion in the XY-plane will be referred to as in-plane water transport. The total water diffusion coefficient ($1.5 * D_{bulk}$) in bulk Nafion for $\lambda = 15$ at $T = 353$ K was found to be 1.93×10^{-5} cm^2/s [65].

Figure 6.10 shows the in-plane water diffusion normalized by the bulk hydrated Nafion water diffusion constant, for different wall hydrophilicities and different film thicknesses. The in-plane water diffusion is noticeably higher for the HH walls ($\varepsilon_{phyl} = 1.20, 1.50, 2.00$) as compared to the LH walls ($\varepsilon_{phyl} = 0.25, 0.50$), for all three different film thicknesses. The cylindrical water channels/micelles in Nafion were found to orient along the hydrophilic substrates and away from the hydrophobic substrates in supported Nafion film experiments [90]. Experimental results further suggested that treated nano-patterned substrates can be used to enhance the directional transport of water within the Nafion membrane since the water transport takes place mostly along the water channels/micelles [90]. A similar enhancement of water transport for the HH walls (substrates) was also observed in the simulations [66].

It is important to keep in mind that the average water cluster sizes decreased significantly for the HH walls. The bulk classical MD simulations of PEMs like Nafion [91], SPEEK [92], PFIA [65] have shown the water diffusion to increase with increasing water cluster sizes and vice versa. However, the capped Nafion films with
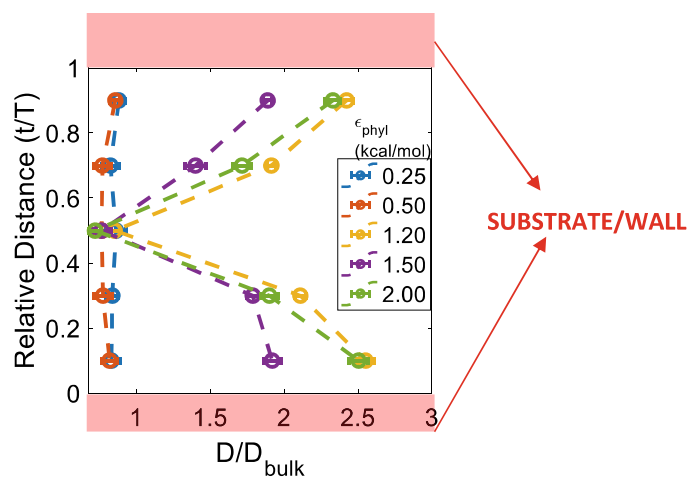
Fig. 6.11 In-plane water diffusion constants (D), normalized by the two-dimensional water diffusion constant (D_{bulk}) at $\lambda = 15$ for bulk Nafion, layer resolved for the 6.3 nm film with varying wall hydrophilicity (ϵ_{phyl}). Relative distance (t/T) is the distance from the bottom of the film (t) normalized by the film thickness (T) [66]

LH walls show much smaller water diffusion than that for the HH walls, despite larger water cluster sizes for the LH walls. This is due to the formation of water channels parallel to the HH walls, in contrast with the long tortuous water channel with bottlenecks in the LH wall films.

The reason behind this enhancement of in-plane water diffusion for the HH walls was further understood by analyzing the water transport in five layers, as shown earlier in Fig. 6.5b. Figure 6.11 shows the layer resolved in-plane water diffusion constant, normalized by the bulk hydrated Nafion two-dimensional water diffusion constant, for the 6.3 nm film. The water diffusion constants for the LH walls are slightly smaller than the bulk hydrated Nafion values. This is probably due to the extreme confinement of the water molecules inside the Nafion film away from the LH walls. For the HH walls, the diffusion constant near the center of the film is close to that for the bulk hydrated Nafion, but the diffusion increases considerably on moving closer to the walls. Similar trends are also observed for thicker films. The presence of such highly mobile water layers near both the HH walls in a capped Nafion film explains the considerably high film averaged in-plane water diffusion constant for the HH walls as compared to the LH walls.

6.4 Atomistic Simulations of Nafion/Graphene Oxide Membranes

Conductivity in polymer electrolyte membranes is significantly affected by water retention. In Nafion and other PFSA-based membranes, ion diffusion takes place at the formed hydrophilic nanochannels [37, 67] and, thus, several studies aiming at the optimization of batteries and fuel cells performance focus on the enhancement of hydrophilicity. In this paragraph, the results have been discussed of the fully atomistic MD simulations of Nafion-based nanocomposite membranes.

The effect of humidification on PFSA membranes has been explored by a variety of experimental techniques such as contact angle measurements [93–95], atomic force microscopy (AFM) [96–99], electrochemical mass-transport measurements [100], and X-ray studies [101]. As was mentioned earlier, it has been observed that at temperatures above 80 °C or at low hydration levels, Nafion membrane conductivity drops significantly. Therefore, the Nafion membrane must be kept sufficiently hydrated in order to retain high proton conductivity levels [37]. In a typical fuel cell, the supplied hydrogen gas is often humidified to enhance proton conductivity. However, the external humidification results in an increase in the size of the fuel cell which is not desirable for portable applications [102]. Another drawback for their use in direct methanol fuel cells (DMFCs) is related to methanol crossover through swelled ionic channels [103].

In order to avoid the need for external humidification and to reduce the methanol crossover effect in DMFCs, self-humidifying membranes doped with inorganic fillers have been examined. Inorganic fillers, such as silica, titania, zirconia, iron oxides, carbon nanotubes, zeolites, and clay, may assist in water retention, enhance proton-conducting properties, and increase mechanical and thermal stability of the membrane [104]. Recently, Nafion/graphene oxide (GO) composites have been explored as potential materials for polymer electrolyte membrane applications [67, 105–109]. The choice of GO stems from properties like large surface area, hydrophilic functional groups, mechanical strength, and chemical stability, which makes it an ideal candidate to form composite membranes [110]. The hydrophilic groups of the GO interact with the protons, which are propagated through the hydrogen bonding network formed with the adsorbed water, allowing for conductivity levels close to 10^{-2} S cm^{-1} [109, 111]. Relevant experiments have shown that the presence of GO modulated the ionic channels of Nafion and decreased the methanol crossover on DMFCs while preserving high ionic conductivity [107].

More detailed studies have demonstrated that the transport of water and other small molecules through graphene-based membranes depends on the interlayer channels and the functional groups of GO [106], like epoxy and hydroxyl groups that may assist water retention due to the formation of a hydrogen bonding network [108, 112]. Investigations of Nafion/GO composites with GOs functionalized with hydrophilic groups, such as $-SO_3H$, $-OH$, and $-NH_2$ [105], supported the idea that functionalization of GO with such moieties facilitates proton transport and enhances the water retention

capability of the Nafion membranes. Pertinent experiments on Nafion/GO composites for DMFC applications [107] attested to their improved properties compared to simple hydrated Nafion membranes. Scanning electron microscopy and transmission electron microscopy studies attributed the enhanced proton conductivity to interactions between the different functional groups in GO and Nafion [108]. The mechanical properties of the Nafion/GO composites as measured by tensile strength experiments [113] were shown to be significantly improved compared to the performance of pristine Nafion membranes, without affecting their swelling properties [108].

GO has also been incorporated in several other composite membranes, like sulfonated polyether ketone [114], PBI [115], polyvinyl alcohol [116], and polyacrylic acid [117, 118] resulting in a marked improvement of their performance. In the case of hydrogels where the water content exceeds 90 wt%, GO may influence in a dramatic manner the physical adsorption of polyelectrolyte chains, the polymer dynamic response at local and global length scales, the charge distributions around the components, and the mobility of the counterions [118]. The vehicular diffusion of water molecules in the presence of GO as studied through MD simulations was found to be slower due to the hydrogen bonding interactions between water molecules and hydroxyl groups of GO [67, 119].

MD simulations, particularly in the fully atomistic representation, allow the study in atomistic detail of structural features and translational dynamics of water and hydronium cations in the formed Nafion channels. The degree of hydration (λ) of the membrane is usually determined by the number of water molecules per side-chain pendant of Nafion. At $\lambda \geq 3$, the sulfonic group loses its hydrogen and so hydronium ions arise [71, 120].

In a recent molecular-dynamics (MD) study [67], the structure and diffusion properties in Nafion/GO systems at three different λ values, i.e., 10, 15, and 20, were simulated. In this work, three different temperatures were examined, i.e., 250, 300, and 350 K at a pressure of 1 bar. The Nafion structure was equilibrated by annealing at 1000 K, while a cooling rate of 50 K/30 ns to the target temperatures was used [67]. More details about the simulation protocol and parameters are given in [67].

In Fig. 6.12, the snapshots of a typical Nafion/GO system are shown, consisting of Nafion, hydronium, water, and GO entities, at $\lambda = 15$, and $T = 300$ K. Differences with respect to the bulk water structure and the formation of water channels can be observed (Fig. 6.12a), a phenomenon that is independent of the presence of the GO in Nafion membranes [65, 67]. As indicated in Fig. 6.12b, the concentration of water onto the GO surface is lower compared to that at distances far from the surface. This results in a lower degree of solvation of the hydronium ions, which are physically adsorbed on the GO flake.

Morphological characteristics related to the spatial arrangement of the different components close to the GO surface were probed by calculating the relevant density profiles, along a direction normal to the GO flake, as shown in Fig. 6.13. It can be observed that the concentration of water on the surface is low, exhibiting a depletion layer. For all λ values examined, a peak is present at a distance close to 8 Å from the surface. It appears that as the hydration level becomes higher, water retention on
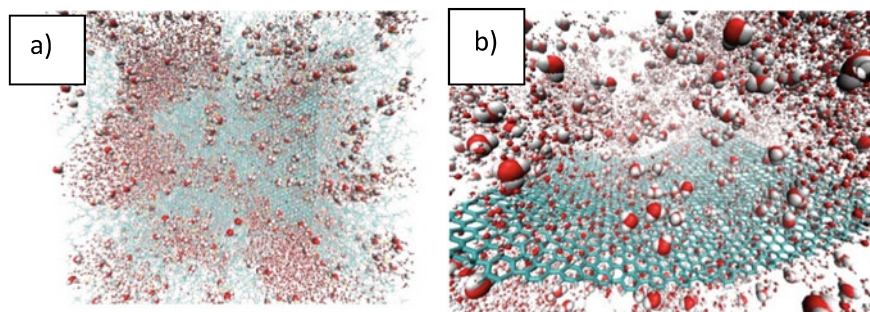
Fig. 6.12 Snapshots [67] of **a** Nafion/hydronium/water/GO and **b** hydronium/water/GO nanocomposite systems. Carbon atoms are shown in dark cyan, oxygen atoms in red, and hydrogen atoms in white
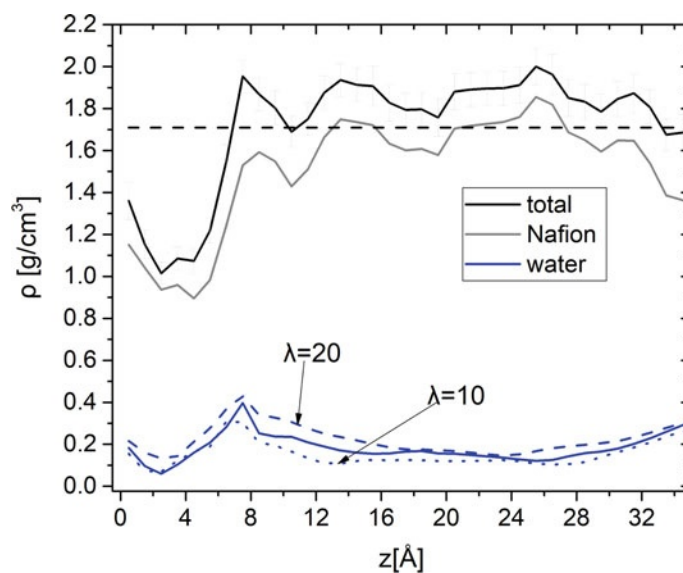

Fig. 6.13 The density profiles along a direction perpendicular to the GO sheet, as a function of the distance from GO surface, for the Nafion/GO systems. The overall density, along with the contributions of Nafion and water, at $T = 300$ K and $\lambda = 15$ is presented. The black dash line depicts the average density of the respective GO-free Nafion system. Water profiles for hydration levels of $\lambda = 10$ (blue dot line) and $\lambda = 20$ (blue dash line), at $T = 300$ K are shown as well. Reprinted with permission from [67]. © 2019 American Chemical Society

the GO tends to increase. On the other hand, the concentration profile of hydronium ions is more uniform (see Fig. 6.3 of [67]). The profile of the Nafion chains shows a reduced concertation close to the GO surface, while the width of the depletion zone of the polymer chains close to GO is commensurate to the size of the side chains [67]. Since the backbone polymer dynamics is expected to be practically frozen at
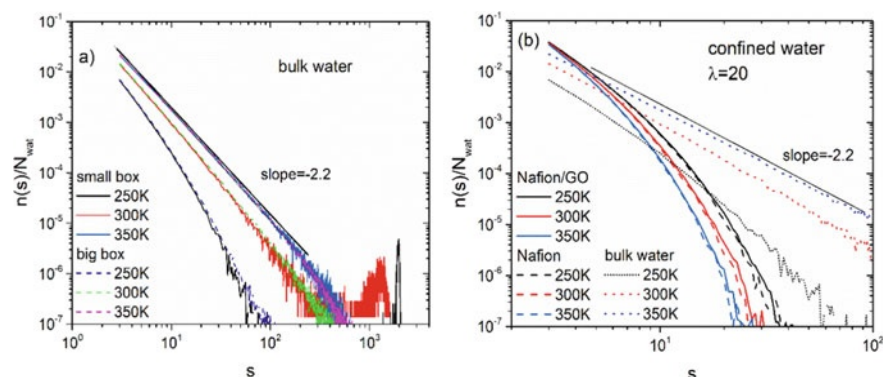
Fig. 6.14 Number of water clusters, $n(s)$, normalized by the total number of water molecules, N_{wat}, as a function of the cluster size, s. **a** Bulk water cluster distributions at the examined temperatures at two different boxes, with sizes of $L \approx 41$ Å (denoted as small box) and $L \approx 126$ Å (denoted as big box) and **b** distributions in Nafion/GO/water and Nafion/water systems are compared with those in bulk water. The straight dash lines indicate a slope of -2.2. Reprinted with permission from [67]. © 2019 American Chemical Society

temperatures below 400 K [103], only the relaxation of the hydrophilic side groups is probed by the MD simulations at the examined temperatures.

Another aspect related to the morphology of the formed channels and the conductivity mechanisms in Nafion membranes is the clustering behavior of water molecules [121]. Since the degree of spatial confinement of water molecules is expected to vary depending on the local environment, it worths studying whether different levels of confinement affect its clustering characteristics under different confinement levels becomes of interest. Such a study was performed in the systems of [67] using the DBSCAN algorithm [122]. In this case, the critical radius for the identification of clusters was taken to be 2.8 Å, based on the location of the first peak of the water–water pair radial distribution function (RDF) [67]. Figure 6.14a depicts the clustering behavior for two different sizes of the simulation box in pristine water systems from the aforementioned study. It is shown that the observed behavior was not affected by finite size effects at the examined sizes of the simulation boxes.

Apart from that, it should be noticed that at all temperatures, the highest probability for cluster formation corresponds to a minimum number of three molecules participating in a cluster (s). As the temperature drops, DBSCAN analysis shows that the size of the largest clusters reduces. Moreover, the distribution of the cluster size follows a power law which is in close agreement with the universal exponent of -2.2, as predicted by the Fisher droplet model [123]. The cluster distribution under confined conditions (i.e., in Nafion-based systems) is shown in Fig. 6.14b. Evidently, the bulk water structure is disrupted. The RDF arising from the centers of mass of water molecules in bulk and under confined conditions (not shown here) remains qualitatively the same (in terms of the number and the position of peaks [67]), but
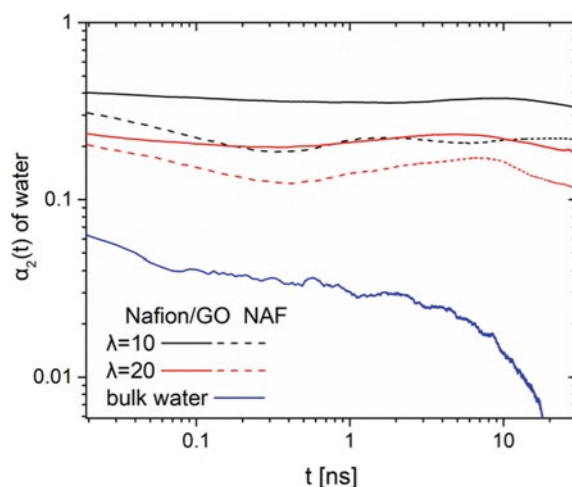
Fig. 6.15 Non-Gaussian parameter [$\alpha_2(t)$] of the water diffusion, in water/Nafion/GO (Nafion/GO) and water/Nafion (NAF) systems (λ equal to 10 and 20) and bulk water, at 300 K. Reprinted with permission from [67]. © 2019 American Chemical Society

the height of the first peak, which relates to the first neighbor shell, becomes higher as the water concertation reduces (i.e., the degree of confinement increases).

Figure 6.15 depicts the non-Gaussian parameter [NGP or α_2 (t)], of the centers of mass water molecules in the examined systems, defined as.

$$\alpha_2(t) = \frac{3\langle\Delta r(t)^4\rangle}{5\langle\Delta r(t)^2\rangle^2} - 1,$$ (6.4)

where $\Delta r(t)$ is the displacement of the center of mass from the original position, at time t. Square brackets denote time and ensemble average. NGP essentially provides a measure for the degree of dynamic heterogeneities in the diffusional motion of the probed particles. It takes the minimum theoretical value (-0.4) when all centers of mass travel the same distance, a value of 0 when Brownian diffusion is at work and values higher than 0 when the distances traveled after time t by the particles under examination are not Gaussian distributed. The latter case denotes an increased level of heterogeneity in the particles' translational motion. According to this picture, it appears that heterogeneities in the water diffusion increase as λ decreases. This becomes more pronounced following the inclusion of GO in the Nafion membrane. In addition, the $\alpha_2(t)$ parameter under confined conditions appears almost an order of magnitude higher compared to the bulk, unconfined case.

This behavior is consistent with the heterogeneous dynamics of water molecules related to the confined motion within the channels formed by Nafion. In the presence of GO, additional constrictions are imposed close to the GO surface due to specific interactions of water molecules (i.e., hydrogen bonding) with the oxidized carbon groups of GO.

More details regarding the characteristics of water translational motion in the microenvironment formed in the Nafion-based systems can be obtained by studying relevant structural relaxation processes which take place within specific spatial dimensions. Such spatiotemporal resolution in molecular motion can be probed by the self-part of the intermediate scattering function, defined as [124]:

$$F_s(q,t) = \left\langle \exp\left(i\vec{q} \cdot \left[\vec{r}_i(t) - \vec{r}_i(0)\right]\right)\right\rangle \tag{6.5}$$

where $\vec{q}$ is the scattering vector, and $\vec{r}_i(t)$ is the position vector of the examined particle (here pointing to the center of mass of a water molecule) at time t. In order to fit the behavior of the intermediate scattering function, the modified Kohlrausch–Williams–Watts (mKWW) expression [125, 126] was employed for a constant magnitude q of the scattering vector,

$$F_s(t) = \alpha_1 \exp\left[-\frac{t}{\tau_1}\right] + (1 - \alpha_1)\exp\left[-\left(\frac{t}{\tau_2}\right)^{\beta}\right]. \tag{6.6}$$

The mKWW fitting function assumes the first term of a simple exponential (i.e., a Debye process) and the second term of a stretched exponential relaxation [125]. The assumption of a Debye relaxation is consistent with the existence of an Arrhenius component of the diffusion in the glassy region [127]. The decorrelation times are calculated, based on the fitting parameters and the expression for the decorrelation time,

$$\tau_c = a_1\tau_1 + (1 - a_1)\left(\frac{\tau_2}{\beta}\right)\Gamma\left(\frac{1}{\beta}\right), \tag{6.7}$$

where Γ is the gamma function. In Fig. 6.16, results for the intermediate scattering function are presented, based on the motion of the center of mass of water molecules in pristine water and the two extreme hydration levels studied in the composite systems. As the evaluation of the dynamics close to the Fickian regime, at $T = 250$ K, is rather ambiguous, especially for the Nafion/GO systems, water translational dynamics is only presented for a wave vector representing a length scale commensurate with the dimensions of the simulation box, i.e., $q = 0.22$ Å^{-1} [85].

The results indicate a more sluggish diffusion as the degree of the water confinement increases. The activation energies were calculated to be 7.3, 10.0 and 11.3 kJ/mol for the bulk water and the water in Nafion/GO with $\lambda = 20$ and in Nafion/GO with $\lambda = 10$ systems, respectively. The common interpretation [126] of the increase observed in the activation energy is the presence of heterogeneities, that is an indication of cooperative diffusion, which was implied earlier by the behavior of the NGP (Fig. 6.15). It is noteworthy that the dynamics of water in the confined conditions exhibits an Arrhenius behavior. An interpretation of the apparent Arrhenius behavior under conditions of cooperative diffusion was provided recently, on the basis of an extension of the super-Arrhenius region [127, 128].
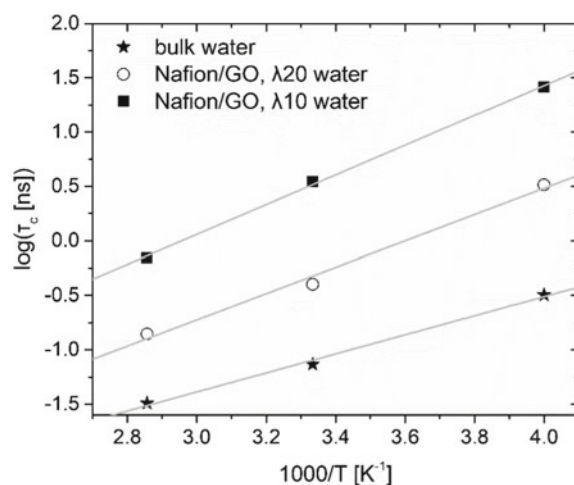
Fig. 6.16 Decorrelation times of the incoherent dynamic structure factor (6.2), $q = 0.22$ Å^{-1}, for water molecules at 300 K. The different symbols refer to the bulk state and to the Nafion/GO systems at $\lambda = 20$ and $\lambda = 10$. Reprinted with permission from [67]. © 2019 American Chemical Society

Apart from the translational dynamics of hydronium ions and the Grotthuss mechanism, the conductivity in the Nafion-based nanocomposite membranes also depends on the adsorption/desorption mechanism of the hydronium ions from the GO surface. This process can be explored by means of a relevant correlation function [117]:

$$h(t) = \frac{\langle g(t)g(0) \rangle}{\langle g^2 \rangle} \qquad (6.8)$$

where $g(t)$ assumes a value of 1 if an adsorption event is detected at time t and 0 otherwise. Angle brackets denote averaging over all pairs and time origins. As a criterion for adsorption of a hydronium ion onto the GO surface, it was taken that the distance between a hydronium oxygen and a hydroxyl hydrogen of GO at time t was less or equal to a critical distance of 3.7 Å, which corresponds to the first peak of the respective RDF function [67]. The critical distance is practically the same as in the case of the sulfur–hydronium interaction. The results presented in Fig. 6.17 were fitted by the mKWW function (6.6).

The desorption times were evaluated to be 5×10^7, 6×10^6 and 1×10^6 ns for hydration levels of $\lambda = 10$, $\lambda = 15$ and $\lambda = 20$, respectively. The results emphasize the significance of the hydration level on the hydronium interfacial dynamics. At $\lambda = 10$, the desorption time is an order of magnitude larger compared to those at higher hydration levels. Only at $\lambda = 20$, the cations desorb from the GO at times close to 1 ms. It should be noted that the average residence time of the water and hydronium ions on the sulfur group of the Nafion is of the order of ps and ns, respectively [129], although cases of hydronium bound to SO_3^- for longer times (approximately 1 ms)
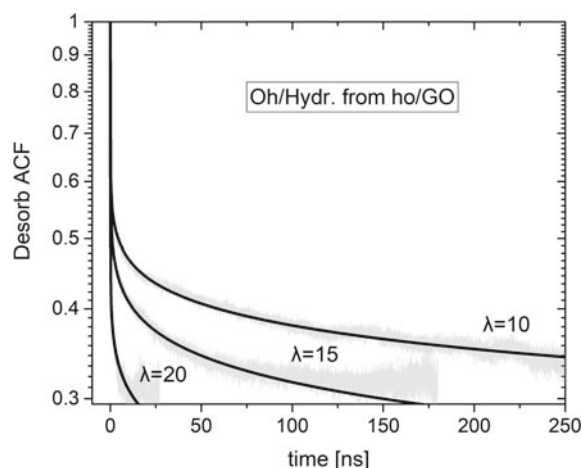
Fig. 6.17 Desorption autocorrelation function (6.8) of the oxygen (Oh) of hydronium ions from the hydrogen (hO) of the GO hydroxyl. Reprinted with permission from [67]. © 2019 American Chemical Society

had also been observed [129]. The deviation in the desorption times between GO and Nafion sulfur groups should be attributed to the low concentration of water near the GO, especially at the hydration levels of $\lambda = 10$ and $\lambda = 15$. Based on the above analysis, it can be concluded that water retention at the Nafion/GO interface appears only at high enough hydration levels of Nafion [67].

6.5 Modeling of Doped Non-humidified Membranes

A few computational studies have been performed on benzimidaozle (BIM)-based membranes. Pahari et al. [130] investigated the structure and dynamics of phosphoric acid-doped PBI membranes at a varying concentration of phosphoric acid using classical MD simulations. The authors observed no phase separation, and phosphoric acid molecules form inter and intramolecular hydrogen bonds at all concentrations of PA. Pahari and Roy [131] employed MD simulations on PA-doped PBI and ABPBI. The authors showed that ABPBI has more affinity toward phosphoric acid as compared to PBI due to the larger number of H-bonds in ABPBI than in PBI. Shirata and Kawauchi [132] employed DFT calculations to examine the interaction of PA with BIM with different configurations. The authors explored several interactions and concluded that *N*-type interactions are the strongest (followed by O–, OH–, and π-type). However, PBI is preferred due to the loss of the mechanical strength of ABPBI with increasing concentration of phosphoric acid. Another drawback of ABPBI membrane is its poor solubility in common solvents employed for membrane casting methods [133]. Also, PA-doped PBI membranes have disadvantages like leaching and condensation

of phosphate groups at high temperatures [134]. Hence, alternatives to PA such as ionic liquids (ILs) are potentially interesting.

Iojoiu and coworkers [54] proposed that the triethylamine (TEA) saturated and (TEATF)-doped Nafion membranes consist of nanoaggregates comprised of proton acceptor and proton donor sites. The authors proposed three possible long-range proton transport mechanisms, (a) via cationic clusters, (b) via a concerted interaction between cation and anion clusters, and (c) via direct proton exchange between cationic and anionic clusters. Kumar and Venkatnathan [135] employed quantum chemistry calculations on IL-doped PFSA membrane for high-temperature fuel cells. The authors used DFT method with B3LYP/6–311++G** basis set for all the calculations. The authors explored several proton transport pathways in a triethylammonium-triflate (TEATF) IL-doped Nafion membrane. In TEATF-doped PFSA membranes, both the cation and anion can access suitable sites, simultaneously, on the sulfonic acid end groups. For example, the cation approaches toward the O atom, and the anion approaches the H atom. The anion abstracts the proton from the acid and facilitates the cation to electrostatically bind to the sulfonate end groups of the membranes. Figure 6.18a shows the structure of the resultant complex, a side-chain fragment of a Nafion membrane with a TEATF.
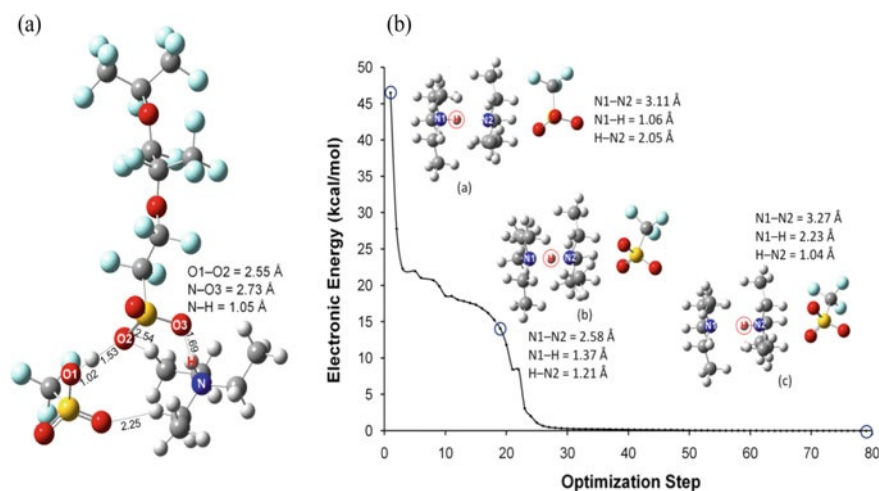

Fig. 6.18 **a** Interaction of a Nafion® side-chain fragment with a TEATF ionic liquid unit. TFA approaches toward hydrogen atom and TEAH$^+$ toward the oxygen atom of the sulfonic acid end group of the membrane fragment. **b** Mechanism of proton transfer in a TEAH$^+$ $\cdots$ TEA $\cdots$ TFA$^-$ complex (**b**) shows the optimization process of TEAH$^+$ $\cdots$ TEA $\cdots$ TFA$^-$. The structures shown in the figure are the configurations of the complex at the points denoted by blue circles, and the moving hydrogen atom is denoted by a red circle. A steep decrease in system energy occurs due to TFA$^-$ interaction with the TEAH$^+$ $\cdots$ TEA complex. The authors showed that the transfer of a proton from a tertiary amine cation to a tertiary amine (see panel b) occurs only on interaction with anion. The interaction of anion with amine increases the basicity of the latter and facilitates the transfer of proton from cation to neutral amine. Reprinted with permission from work of Kumar and Venkatnathan [135]. © American Chemical Society

A high boiling point (256 °C) of imidazole (compared to water) makes them promising materials as proton carriers in high-temperature fuel cells. Hydrogen bonding in imidazole plays a key role in proton conduction and rotation of an imidazole molecule in the process results in the cleavage of hydrogen bonds between molecules. In another quantum chemistry study, Kumar and Venkatnathan [136] explored proton transport and rotation energy barrier in imidazole chains. The authors showed that the propagation of an excess proton along the imidazole chain occurs with energy barriers lower than 1 kcal/mol. The authors calculated the energy barriers for rotation of imidazole molecules in two, three, and four imidazole molecule chains and found that the barrier is equal to the number of hydrogen bonds broken in the process. Figure 6.19 shows the change in structure and potential energy of a chain of three imidazole molecules with the rotation of an imidazole molecule. The rotational barrier in two imidazole chain is 8.0 kcal/mol, in three imidazole chain, it is 17.1 and 20.0 kcal/mol in four imidazole chain.
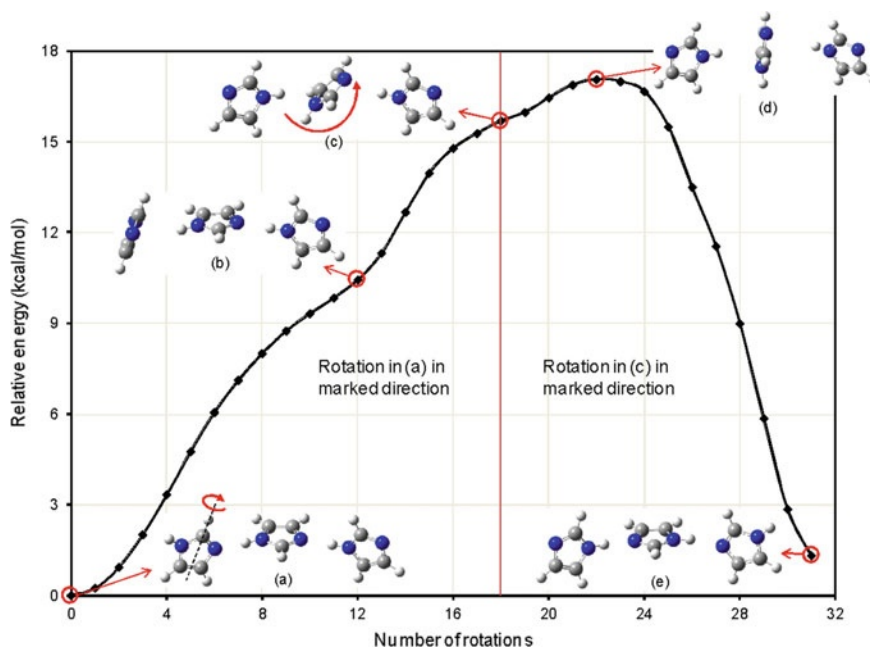

Fig. 6.19 A PES of 3-imidazole-molecule chain. The scan is separated into two parts: left part is due to rotation of first imidazole in structure (**a**); and right part is due to rotation of second imidazole in structure (**c**). The rotation steps, in the marked directions, were chosen as 10° and 9.7°, respectively. Structure (**b**) shows that up to 120° rotation, there is no effect on hydrogen bonding between second and third molecule. Structure (**d**) shows maxima in which the second molecule is showing minimum interaction with other molecules. In structure (**e**), all imidazole molecules are flipped. Reprinted with permission from work of Kumar and Venkatnathan [136]. © American Chemical Society

In a different study, Venkatnathan and coworkers [137] explored proton transport pathways in base-rich imidazolium ionic liquids. The authors suggested proton transport pathways to explain the experimentally observed enhanced conductivity in base-rich PILs. The results showed the barrierless rotation of imidazole in base-rich ionic liquids, could be one of the possible reasons for enhanced conductivity. The figure illustrates the overall mechanism of proton transport in imidazole rich IL. Figure 6.20 illustrates the overall proposed mechanism of proton transport in one such system and suggests barrierless rotation of imidazole molecule to be the reason for the enhanced conductivity of base-rich ILs.

The addition of triflic acid, which exist in its dissociated form (TFA), is known to enhance the efficiency of PA-doped ABPBI membranes. Sunda et al. [138] employed MD simulations to characterize the structure and dynamics of ABPBI + PA as shown in Fig. 6.21, ABPBI + TFA and ABPBI + PA + TFA blends with varying levels of hydration. The structural properties such as RDFs showed that the distance between two adjacent imidazole units on the polymer chain remains unaffected by hydration and the type of blend. The end-to-end polymer chain distance and radius of gyration are also unaffected by hydration and the type of blend, illustrating that the stability of polymer membranes under various hydrated acidic environments remains unaffected. The number of PA, TFA, and water molecules in the cluster around the
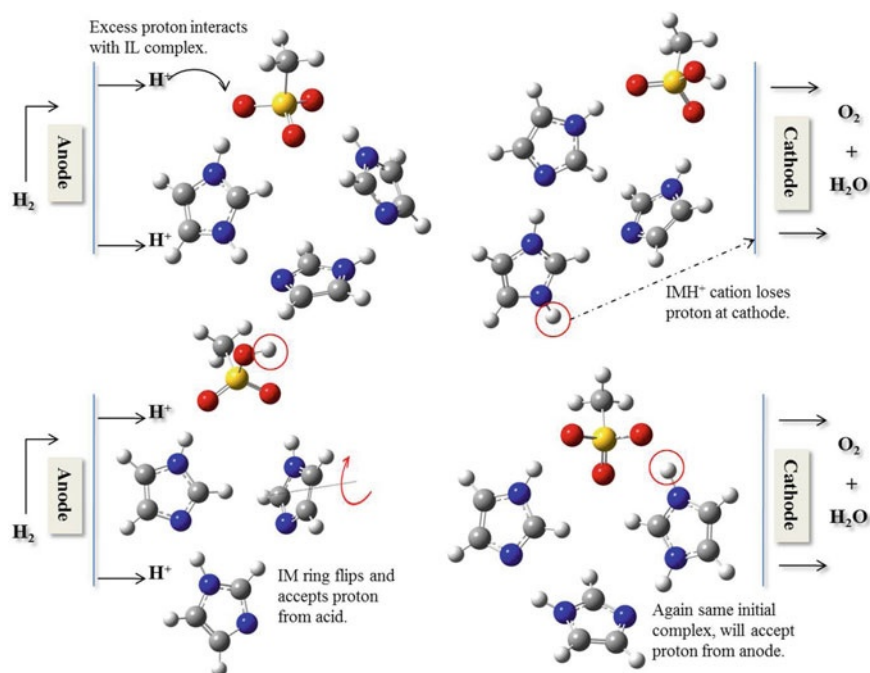

Fig. 6.20 Schematic of proton transport pathway in [MSA]/[IM] = 1:3, i.e., IMMSA with two IM molecules. Reprinted with permission from Venkatnathan and coworkers [137]. © American Chemical Society
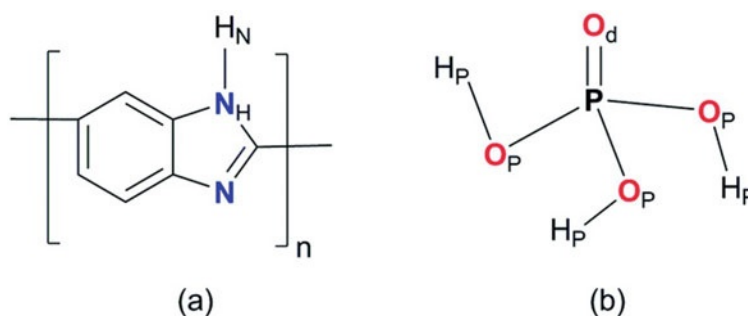
Fig. 6.21 Chemical structure with atom types of **a** ABPBI polymer membrane and **b** phosphoric acid (PA). © Royal Society of Chemistry

polymer membrane (skewed and extended form) is found to depend significantly on the extent of hydration. The lowest water mobility was obtained from the ABPBI + PA + TFA blend, which suggests that this blend could be the most effective in reducing acid leaching from the membrane matrix.

In a different study, Venkatnathan and coworkers [139] performed MD simulations to examine structure and dynamics in neat BIM, phosphoric acid, and PA-BIM mixtures. The authors observed that diffusion coefficients of BIM decrease with increasing phosphoric acid concentration, whereas the diffusion of PA increases. The RDFs showed a strong hydrogen bonding interaction between the imine N of BIM and hydrogen of phosphoric acid. Further Venkatnathan and coworkers [140] employed MD simulations to characterize the effect of polymer chain length using a dimer to 100-mer. Results from simulations (dimer to decamer) showed the following trends: the inter-chain and intra-chain interactions in the membrane are unaffected with polymer chain length and temperature, though a significant increase with PA doping is observed. The radius of gyration linearly increases with polymer chain length and remains unchanged with PA doping and temperature. However, the end-to-end distance deviates from linearity with polymer chain length which suggests increased coiling of the membrane. The diffusion coefficient of PA increases with PA doping and temperature but remains constant with polymer chain length. The activation energy of diffusion of PA decreases significantly with an increase in polymer chain length at low PA doping but remains unaffected at higher PA doping. The authors proposed decamer to be optimal chain length to calculate various structural and dynamical properties.

6.6 Mesoscopic Simulations and Simulated Example: SPEEK Membrane

In this section, two examples of the mesoscopic modeling of polymer ion-exchange-based membranes will be considered. Since the average size of the polymer

membrane domains is about 4 nm, it seems rather attractive to use the mesoscopic simulation methods to model the morphology of such systems. These methods allow us to study samples of PEM membranes with a characteristic scale of 20–100 nm over long-time intervals of 1–1000 μs. This is achieved by abandoning atomistic detail when moving to a larger scale using collective variables. To model a SPEEK based membrane with different water content, the mesoscale DDFT simulations (MDDFT) [141] and dissipative particle dynamics [142] methods were used. Although these methods are based on the use of different simulation principles, they are united by a common approach to the construction of coarse-grained models.

MDDFT method is based on a dynamic version of the density-functional theory in combination with the Flory–Huggins model. As collective variables, it uses fields of the number particle densities $\rho_\alpha(\mathbf{r}, t)$. The evolution of density fields can be found by solving a system of diffusion Langevin equations. All details of the method are set out in [76, 141, 143–146].

DPD method is another mesoscale simulation technique proposed initially by Hoogerbrugge and Koelman [142, 147] and generalized later to molecular systems [148]. As in the MD method, the evolution of the coarse-grained particles is described by the system of Newton equations of motion. One can treat as an advantage the fact that both MDDFT and DPD methods use the same strategies for building the mesoscopic models of the molecular systems and evaluating the force parameters through the Flory–Huggins parameters [149]. In MDDFT and DPD method, the simulated system is placed in a cell of a fixed volume V with periodic boundary conditions. All molecular objects are replaced by some equivalent set of beads, called mesoscopic particles (MPs) of various types α. They all have the same volume $v_\alpha \equiv v$. Each of the subsystems corresponds to a selected sequence of structural units of the macromolecule chain (these can be its individual segments), or to a certain number of solvent molecules. The choice of volume v is determined by the parameterization of the system, which, in turn, determines its degree of coarsening. It introduces a unit scale $\sigma = (6v/\pi)^{1/3}$. In MDDFT, polymer chains have the same Gaussian coil conformation, and the spatial distribution of MP can be described by the potential field of local densities $\rho_\alpha(\mathbf{r}, t)$. Unlike MDDFT, the DPD method imposes no restrictions on the conformational mobility of the polymer chains and describes the structure of the polymer systems more accurately.

Consider the process of constructing a coarse-grained model for the sulfonated PEEK, poly(oxy-1,4-phenyleneoxy- 1,4-phenylenecarbonyl- 1,4-phenylene), (SPEEK) [11, 77] (Fig. 6.22). To construct a mesoscopic model of SPEEK based membrane, it is necessary to correctly map the atomistic model of the ionomer chain to the equivalent coarse-grained representation in the form of a sequence of repeating mesoscopic particles and to subsequently calculate the interaction parameters between these MPs based on Flory–Huggins parameters [149]. Although SPEEK can be considered a random block copolymer, for simplicity, the composition and structure of the chains was represented as $[A_n B_m]_N$, where n and m are the number of polar and non-polar beads, N is the number of the chain blocks. The $n{:}m$ ratio allows to characterize the degree of sulfonic acid (DS) of the polymer. Analysis of the features of the chemical structure of the polymer and the requirement to
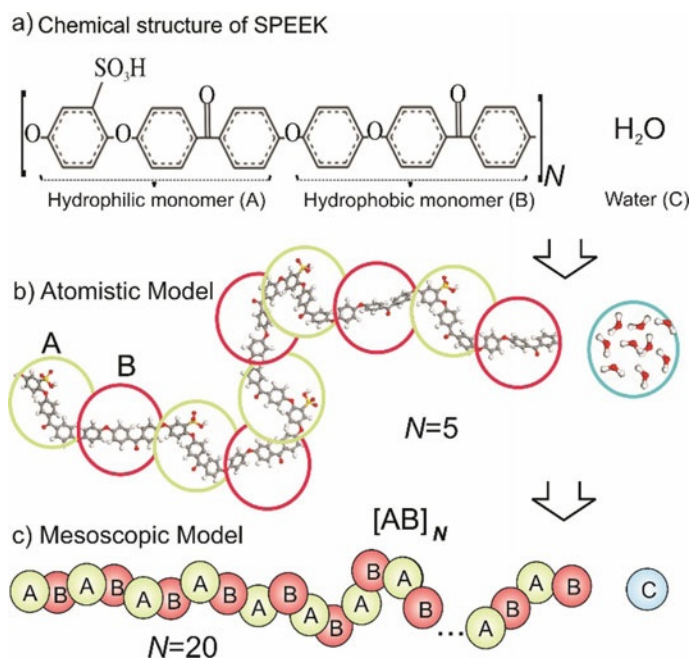
Fig. 6.22 Mapping of a fragment of sulfonated poly(oxy- 1,4-phenyleneoxy- 1,4-phenylenecarbonyl -l,4-phenylene) chain and a cluster of water molecules onto the equivalent mesoscopic representation

comply with the structural characteristics of the model (contour length, rigidity and distance between the ends of the chain) allows to select the size of the statistical segment a of the basic chain,

$$a = C_\infty L_{\mathrm{mon}}, \qquad\qquad (6.9)$$

where $C_\infty = 3.36$ is the characteristic ratio (characterizes the rigidity of the chain), L_{mon} is the size of the monomer. Estimates for C_∞ were done using the Bicerano method [77, 150]. These results indicate a higher degree of conformational mobility of the PEEK chains in comparison with Nafion and its $C_\infty = 7.13$ [76]. Aromatic rings were chosen as the basic fragment of the SPEEK chain, which gives $L_{\mathrm{mon}} = 5.3$ Å (the size of the benzene ring). Based on the L_{mon} and C_∞ values 6.9 defines the length of the statistical segment $a = 17.8$ Å, that is close to the length of the sulphonated and non-sulphonated comonomers in SPEEK (13.5 Å). Thus, chains of SPEEK can be matched with mesoscopic particles (MPs or beads) of two types A and B of the same size. The volume of MP can also be estimated by the Bicerano method, which gives $v = 250\,\mathrm{cm}^3/\mathrm{mol}$. Mesoscopic particles of the third type (C) are matched to water molecules. Given the value of v, one MP of water corresponds to

about 14 molecules. The mapping of the system to a coarse representation is shown in Fig. 6.22.

To determine the parameters of the intermolecular interactions $\varepsilon_{\alpha\beta}$ used in MDDFT [141] and $a_{\alpha\beta}$ used in DPD [142], it is necessary to calculate the Flory–Huggins parameters $\chi_{\alpha\beta}$ for the A, B and C mesoscopic particles, which are related to the Hildebrand solubility parameters δ_α as

$$\chi_{\alpha\beta} = \frac{\nu(\delta_\alpha - \delta_\beta)^2}{RT} - \chi_s, \tag{6.10}$$

where χ_s is the entropy contribution to the free energy of mixing, R is the gas constant. The contribution of χ_s can be neglected since its estimates for many polymer/solvent blends give the result of 0.34 [151, 152], which is only a small correction to the first term in 6.10. The values of the parameters δ_α can be obtained via the cohesion energy density E_{coh}/V:

$$\delta_\alpha = \sqrt{E_{\mathrm{coh}}^{(\alpha)}/V} \tag{6.11}$$

The estimates of δ_α can be obtained using the Bicerano [150] and Askadsky [153] methods. The MD-based calculations give a more accurate value of δ. The value of $E_{\mathrm{coh}}^{(\alpha)}$ is equal to the change in the potential energy of a single volume of a substance when all intermolecular forces are turned off. It characterizes the intensity of the interatomic and intermolecular interactions. In other words, E_{coh} shows the change in the potential energy of the system during the transition of molecules into the gas phase from the condensed state. The analysis performed in [77] allows us to choose the parameters δ_α and to determine the following values for the Flory–Huggins parameters: $\chi_{AB} = 21.6$, $\chi_{AC} = 1.32$, and $\chi_{BC} = 33.6$.

In the framework of MDDFT, three SPEEK/water systems have been studied in detail with different degree of sulfonation (DS) of the polymer matrix. DS is regulated by the composition of the polymer chain $[A_n B_m]_N$. The length of the chains in all cases has the same value $(n + m)N = 40$. The following compositions are studied: $[A_1 B_1]_{20}$ (DS $= 50\%$), $[A_3 B_2]_8$ (60%), and $[A_3 B_1]_{10}$ (75%). In all calculations, the fixed temperature was used, $T = 298\ K$.

The second main parameter of the calculations is the amount of water in the membrane, which is governed by λ; it was varied from 0.5 to 14 to change the hydration level. The amount of water in the membrane is convenient to control using the water volume fraction φ_C, which corresponds to the ratio of the number of mesoscopic water particles to the total number of particles in the system. The solutions to the system of MDDFT equations are searched on a grid of $32 \times 32 \times 32$ nodes with a step of 1 nm. This gives the modeling cell edge of the size of 32 nm. This step is chosen according to the unit length of 0.92 nm, calculated based on the estimate of the base volume ν of the mesoscopic particles.

In Fig. 6.23, the isocontour plot of the distribution of local densities ρ_C of the water MPs at the volume section $V(x, y, 0)$ is performed for three values of DS at
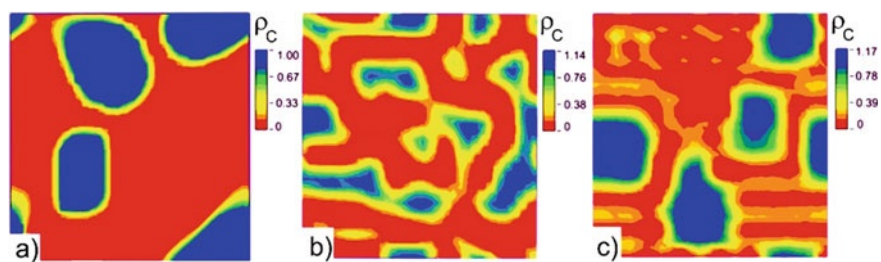
Fig. 6.23 The density distribution $\rho_C(\mathbf{r}, t)$ of the MPs of water on the section plane $V(x, y, 0)$ at the same volume fraction $\varphi_C = 0.29$ of water in the membrane: **a** $[A_1B_1]_8$ ($\lambda = 11$); **b** $[A_3B_2]_8$ ($\lambda = 9.5$); **c** $[A_3B_1]_8$ ($\lambda = 7.6$)

$\varphi_C = 0.29$. In the system with the lowest degree of sulfonation in the case of $[A_1B_1]_8$ chain in the final state, the water forms isolated clusters separated by an average distance of about 19 nm. The shape of the clusters is close to ellipsoidal, and their cross-section is 10 nm. The interface zone has a clear boundary with a thickness of 0.8 nm.

For higher degrees of sulfonation, DS = 60% ($[A_3B_2]_8$) and 75% ($[A_3B_1]_8$), a channel network connecting water clusters is observed in the model membranes. At the same time, the morphologies of the membranes at DS = 60 and 75% are very different. In Fig. 6.23, it is clearly seen that at DS = 60%, the morphology of water channels looks the most preferable. The water forms rather wide channels in which its average field density has high average values—from 0.5 and higher. The average maximum cross-section diameter is about 8 nm. A comparison of the three membrane samples allows us to conclude that the sequence $[A_3B_2]_8$ is optimal, since one can assume that the membrane will have better transport properties.

The volume visualization of the density distribution of water in the SPEEK membrane for $[A_3B_2]_8$ (Fig. 6.24) shows how the percolation of the water subsystem occurs at different threshold densities ρ_C and λ. The three density values are chosen because the concentration of water in the water channels is highly non-uniform. The largest values of the density of the MPs of water are reached in the center of the water channels. The thickness of the interface zone, where the overlap in the density distributions of subsystems A and C is observed, is about 1.6 nm (Fig. 6.23). The choice of the three values for the threshold ρ_C allows to produce a clearer picture of the water channels percolation in the material as shown in Fig. 6.24. It is seen that the connected network of the water channels is already formed with a low water content, $\lambda = 0.5$, due to the presence of the microphase separation of the hydrophobic and hydrophilic segments of the polymer chain in a dry polymer (Fig. 6.23b).

With an increase in the water content to $\lambda > 1.2$, the presence of the water channels domains with densities $\rho_C > 0.2$ is clearly seen. Many elongated and dumbbell-shaped regions are formed in the membrane as a result of the confluence of the small water domains. An estimate of the percolation threshold λ^* for the number density of water particles $\rho_C = 0.2$ indicates that the water domains begin to form a connected network in the range of $1.2 < \lambda^* < 2.3$, that is, when approximately two
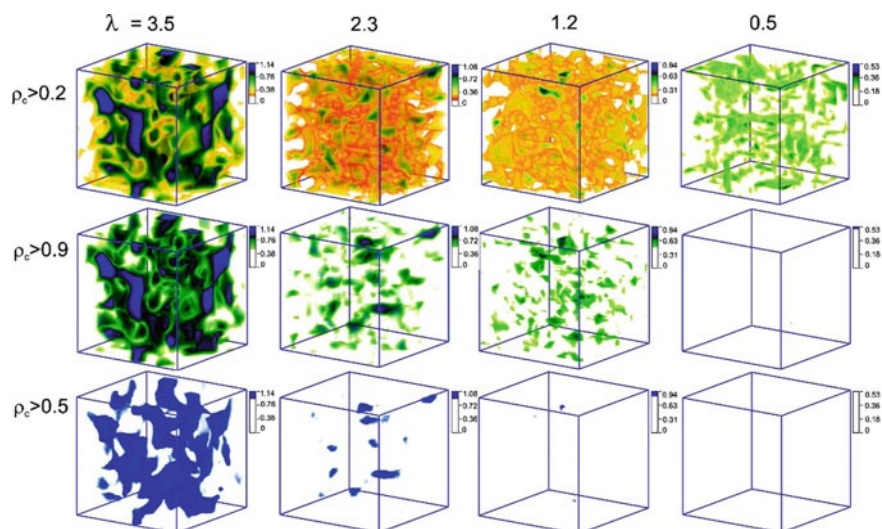
Fig. 6.24 Visualization of the formation of the water channels in the volume of the SPEEK membrane in the case of $[A_3B_2]_8$ monomers sequence, for the different threshold values of ρ_C depending on the water content λ

water molecules correspond to one sulfonic acid group. For other threshold values ρ_C, the following results are obtained: $\lambda^* = 4$ for $\rho_C > 0.5$ and $\lambda^* = 7$ for $\rho_C > 0.9$, which is significantly below the corresponding estimates for Nafion, $\lambda^* = 16$, as obtained in [76].

The low percolation threshold for $[A_3B_2]_8$ chains can be explained by the high degree of sulfonation of the ionomer model chain. The morphology that occurs in the case of $[A_3B_2]_8$ chains is similar to the disordered lamellar phase (Fig. 6.23) for polar and nonpolar domains. Since the volume fraction of the sulfonated MPs in the dry membrane is 60%, the polar domains form a continuous phase. Such a microphase separation is ideal for the fast percolation of the water phase through the membrane at a small λ.

Thus, the small value of the percolation threshold λ^* in the case of $[A_3B_2]_8$ chains is due to the percolation of the polar subsystem. This allows to understand the relatively large value of λ^* for Nafion-1100 in [76]. The degree of sulfonation of Nafion-1100 is 30%, which exactly corresponds to the percolation of randomly distributed homogeneous spheres [154]. However, the spatial distribution of the polymer chain segments strongly depends on their conformational behavior. The percolation threshold for the polar units and, hence, for the water phase may take higher values.

Figure 6.25 shows the dependence of the average maximum diameter D of the channels cross-section on λ. It can be seen that as the volume fraction of water decreases to $\lambda^* \sim 7$ (for areas with $\rho_C > 0.9$), the channels contract only slightly. Thus, the values $\lambda > 7$ should correspond to the stable operation mode for the membrane. However, at $\lambda \leq 7$, a sharp contraction of the cross-section of the channels
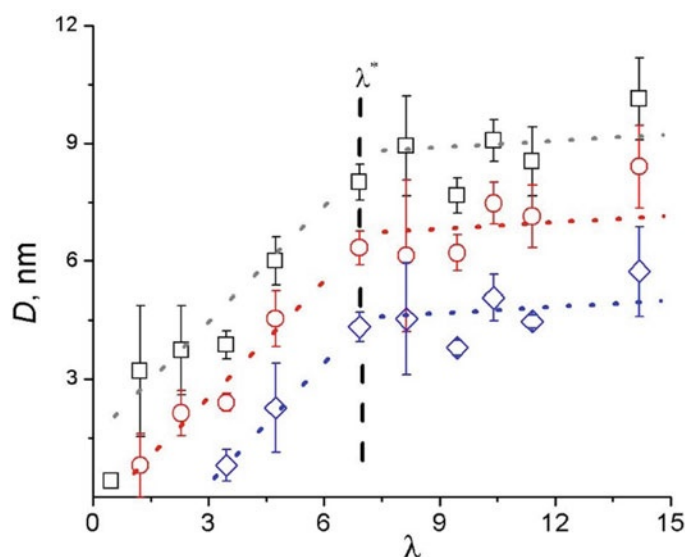
Fig. 6.25 The maximum average diameter D of the cross-section of the water channels as function of the volume fraction of water in case of $[A_3B_2]_8$ chains. The diameters are calculated for the following MP densities: (1) $\rho_C \geq 0.2$; (2) $\rho_C \geq 0.5$; (3) $\rho_C \geq 0.9$. The dotted lines are constructed by linear approximation, λ^* is the percolation threshold

is observed. This behavior is consistent with the behavior of real membranes as a result of water loss at high temperatures. Interesting that at $\lambda \sim 1.5$, when the percolation for water occurs in the system ($\rho_C > 0.2$, see also Fig. 6.24), the maximum cross-section of the channels is $D \sim 2.5$ nm. This fact allows to suppose that SPEEK membrane in the case of $[A_3B_2]_8$ chains can retain its conductive properties even with relatively low water content in the system.

The results of the SPEEK-based ion-exchange membranes simulations show that with a decrease in system hydration, the network of the water channels is broken primarily due to the non-uniform distribution of hydrophilic and hydrophobic domains in the matrix volume. The percolation threshold is higher for more heterogenic domain distribution. It is obvious that the best transport properties can be provided by a material in which, as a result of the microphase separation of polar and non-polar blocks of the polymer chain, the continual distributions of the corresponding domains are formed. In the ideal case, the lowest percolation threshold is demonstrated by ionomers, which in the dry state have the linked network of hydrophilic domains. It can be supposed that the better topology of the structure of the water channels will be demonstrated by ionomers based on diblock copolymers, which contain two types of blocks: (a) susceptible to sulfonation and (b) resistant to H_2SO_4 effect. This statement is confirmed in [155] where the authors changed the degree of sulfonation of the polystyrene block and the total molecular weight of

the polymer chain and succeeded to produce the membranes in which hydrophilic domains of various morphologies are observed.

The optimism for the use of diblock copolymers for the production of PEM is due to the extensive experience in the synthesis of such polymers for the production of mesoporous materials [156]. Depending on the composition of the polymer chain, the stable domains are formed as a result of the microphase separation. The domains form various types of supramolecular packaging, such as lamellar, hexagonal, and cubic. The types of cubic packaging: primitive (denoted as P), double diamond (DD), and gyroid structures (G) are bicontinuous spatial structures. Therefore, the membranes in which such ordering of domains forms as a result of microphase separation, even with low moisture, should have a well-organized network of the water channels. The latter is an important factor for creating high-performance membranes for medium-temperature fuel cells.

To build a model of an ion-exchange membrane, a linear diblock copolymer is used, consisting of N MPs of diameter $\sigma = 1$, interacting according to Hooke's law. The model chain includes the polar (hydrophilic A) and non-polar (hydrophobic B) types of thermodynamically incompatible beads. The chain structure can be written as $A_n B_{N-n}$, where $N = 24$. The ratio of the hydrophobic and hydrophilic beads is regulated by the parameter m, which take values from 1 to 12 ($f = n/(N-n) = 0.04 \div 0.5$). The maximum value of n is limited, since for $n > 12$ the polymer becomes water soluble as the polar beads become dominant. As a chemical prototype of monomers of types A and B, the sulfonated and nonsulfonated SPEEK monomer blocks can be considered. To determine the interaction parameters, the same (as in the DDFT simulations) Flory–Huggins parameters χ_{ij} have been used. To model the membranes, the cubic cell with the edge L and periodic boundaries conditions in all three dimensions was used. For a correct description of the hydrodynamic properties of the system, the average number density should be $\rho = 3$ [148], which corresponds to $3L^3$ mesoscopic particles. The total fraction of all MPs in the system is taken as a unity.

For all the simulated systems, the clear inhomogeneous distribution of the mesoscopic particles is observed. An example of such separation for the $A_5 B_{19}$/water system is shown in Fig. 6.26. It is seen that the water MPs form the cylindrical phase. The hydrophilic phase, as shown in Fig. 6.26a, forms some transition zones with a
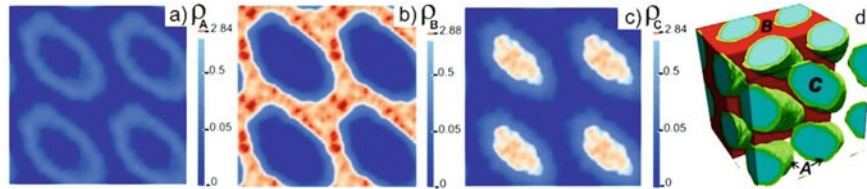

Fig. 6.26 The spatial distribution of the partial average number densities of MPs ρ_α in the $A_5 B_{19}$/water system: at the section $V(x, y, 0)$ for the subsystems: **a** A; **b** B; **c** C. **d** Combined construction for densities $\rho_A \geq 0.5$, $\rho_B \geq 1.75$, $\rho_C \geq 0.75$. $T = 300$ K, $\lambda = 10$, $L = 27\,\sigma$, $t = 100{,}000$ DPD steps
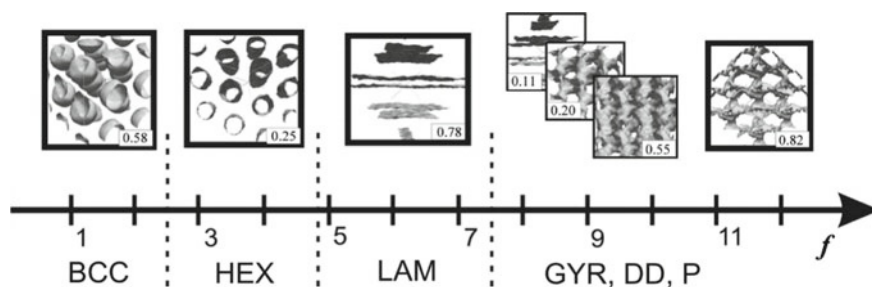
Fig. 6.27 One-dimensional phase diagram of the system A_nB_{24-n}/water ($T = 300$ K, $\lambda = 10$). The vertical lines show the boundaries of the areas of the most frequent occurrence of the following spatial packages: body-centered (bcc), hexagonally packaged cylinders (hex), lamellar (lam), gyroid (G), perforated lamellar (hpl). The examples of snapshots of the simulation cells in the final state demonstrate the boundaries of hydrophobic MPs localization. The isosurfaces are built for $\rho_B = 0.5$

strongly diffused boundary between the subsystems B and C. From the snapshot as shown in Fig. 6.26d, it is obvious that the water clusters form the cylindrical domains with hexagonal packing; they are embedded in the ionomer matrix and covered with a "shell" of hydrophilic beads.

Figure 6.27 presents the results of the calculation of the one-dimensional phase diagram of the structures that occurs most often during the simulations. The most frequently occurring morphologies are those with the largest probability $\omega(f, L)$. It is defined as the ratio of the number of arisen states with a specific type of symmetry to the number of independent calculations performed. For the accurate identification of the structures found, the structural factors are calculated. Among the identified cubic symmetries, the gyroid structure is characterized by the highest probability $\omega(f, L)$ of occurrence; it forms in the case of the A_9B_{15} chains.

The discussed modeling approaches clearly show that with proper selection of the ratio of the lengths of the hydrophilic and hydrophobic blocks in the ionomer chain, there exists a possibility to create a PEM with a penetrating system of the water channels in the entire volume of the membrane sample.

6.7 Summary

In this chapter, the multiscale computer simulations of polyelectrolyte membranes, the very important components of modern fuel cells and flow batteries, have been reviewed. The primary objective of a PEM is to allow protons to pass through it. Additionally, PEMs separate the fuel and air streams in a fuel cell and electrolytes in a flow battery. Detailed density function theory simulations of Nafion membrane doped with triethylammonium-triflate provided insights into the proton transport reaction coordinates. The classical molecular-dynamics simulations of a Nafion film confined by

variable wettability substrates and a Nafion-graphene oxide nanocomposite provided information about the effect of the interfacial interactions in PEM nanocomposites on water clustering and proton diffusion. Finally, the mesoscopic dynamic density function theory simulations of SPEEK membranes revealed the influence of the sulfonation degree on the internal hydrated domain sizes. The MDDFT results on the influence of the amount of PEM hydrophobic and hydrophilic blocks on water cluster morphology have also been discussed.

References

1. L. Carrette, K.A. Friedrich, U. Stimming, Fuel cells—fundamentals and applications. Fuel Cells **1**, 5–39 (2001). https://doi.org/10.1002/1615-6854(200105)1:1%3c5::AID-FUCE5%3e3.0.CO;2-G
2. Wikipedia. Wikipedia (n.d.) https://en.wikipedia.org/wiki/Fuel_cell. Accessed 24 Sept 2019
3. Z. Qi, G.M. Koenig, Review article: flow battery systems with solid electroactive materials. J. Vac. Sci. Technol. B, Nanotechnol. Microelectron. Mater. Process Meas. Phenom. **35**, 040801 (2017). https://doi.org/10.1116/1.4983210
4. P. Antonucci A. Aricò P. Cretì E. Ramunni V. Antonucci, Investigation of a direct methanol fuel cell based on a composite Nafion®-silica electrolyte for high temperature operation. Solid State Ionics **125**, 431–437 (1999). https://doi.org/10.1016/S0167-2738(99)00206-4
5. D.H. Jung, S.Y. Cho, D.H. Peck, D.R. Shin, J.S. Kim, Performance evaluation of a Nafion/silicon oxide hybrid membrane for direct methanol fuel cell. J. Power Sources **106**, 173–177 (2002). https://doi.org/10.1016/S0378-7753(01)01053-9
6. B. Smitha, S. Sridhar, A. Khan, Synthesis and characterization of proton conducting polymer membranes for fuel cells. J. Memb. Sci. **225**, 63–76 (2003). https://doi.org/10.1016/S0376-7388(03)00343-0
7. H. Wang, G.A. Capuano, Behavior of raipore radiation-grafted polymer membranes in H_2/O_2 fuel cells. J. Electrochem. Soc. **145**, 780 (1998). https://doi.org/10.1149/1.1838345
8. R. Nolte, K. Ledjeff, M. Bauer, R. Mülhaupt, Partially sulfonated poly(arylene ether sulfone)—a versatile proton conducting membrane material for modern energy conversion technologies. J. Memb. Sci. **83**, 211–220 (1993). https://doi.org/10.1016/0376-7388(93)85268-2
9. G. Gebel, P. Aldebert, M. Pineri, Swelling study of perfluorosulphonated ionomer membranes. Polymer (Guildf) **34**, 333–339 (1993). https://doi.org/10.1016/0032-3861(93)90086-P
10. J. Kerres, W. Cui, S. Reichle, New sulfonated engineering polymers via the metalation route. I. Sulfonated poly(ethersulfone) PSU Udel® via metalation-sulfination-oxidation. J. Polym. Sci. Part A Polym. Chem. **34**, 2421–2438 (1996). https://doi.org/10.1002/(SICI)1099-0518(19960915)34:12<2421::AID-POLA17>3.0.CO;2-A
11. X. Jin, M.T. Bishop, T.S. Ellis, F.E. Karasz, A sulphonated poly(aryl ether ketone). Br. Polym. J. **17**, 4–10 (1985). https://doi.org/10.1002/pi.4980170102
12. P. Xing, G.P. Robertson, M.D. Guiver, S.D. Mikhailenko, K. Wang, S. Kaliaguine, Synthesis and characterization of sulfonated poly(ether ether ketone) for proton exchange membranes. J. Memb. Sci. **229**, 95–106 (2004). https://doi.org/10.1016/J.MEMSCI.2003.09.019
13. H.-L. Wu, C.-C.M. Ma, C.-H. Li, C.-Y. Chen, Swelling behavior and solubility parameter of sulfonated poly(ether ether ketone). J. Polym. Sci. Part B Polym. Phys. **44**, 3128–3134 (2006). https://doi.org/10.1002/polb.20964
14. R.T.S. Muthu Lakshmi, V. Choudhary, I.K. Varma, Sulphonated poly(ether ether ketone): synthesis and characterisation. J. Mater. Sci. **40**, 629–636 (2005). https://doi.org/10.1007/s10853-005-6300-2

15. N. Agmon, The Grotthuss mechanism. Chem. Phys. Lett. **244**, 456–462 (1995). https://doi.org/10.1016/0009-2614(95)00905-J

16. O. Markovitch, N. Agmon, Structure and energetics of the hydronium hydration shells. J. Phys. Chem. A **111**, 2253–2256 (2007). https://doi.org/10.1021/jp068960g

17. M. Eigen, L. de Maeyer, Self-dissociation and protonic charge transport in water and. Proc. R. Soc. Lond. Ser. A Math. Phys. Sci. **247**, 505–533 (1958). https://doi.org/10.1098/rspa.1958.0208

18. G. Zundel, J. Fritsch, *The Chemical Physics of Solvation.* vol. 2 (Elsevier, 1986). https://doi.org/10.1016/0166-1280(87)85076-5

19. M. Tuckerman, K. Laasonen, M. Sprik, M. Parrinello, *Ab initio* molecular dynamics simulation of the solvation and transport of hydronium and hydroxyl ions in water. J. Chem. Phys. **103**, 150–161 (1995). https://doi.org/10.1063/1.469654

20. M.E. Tuckerman, K. Laasonen, M. Sprik, M. Parrinello, Ab initio simulations of water and water ions. J. Phys. Condens. Matter **6**, A93-100 (1994). https://doi.org/10.1088/0953-8984/6/23A/010

21. P.V. Komarov, P.G. Khalatur, A.R. Khokhlov, Large-scale atomistic and quantum-mechanical simulations of a nafion membrane: morphology, proton solvation and charge transport. Beilstein J. Nanotechnol. **4**, 567–587 (2013). https://doi.org/10.3762/bjnano.4.65

22. M.K. Petersen, G.A. Voth, Characterization of the solvation and transport of the hydrated proton in the perfluorosulfonic acid membrane nafion. J. Phys. Chem. B **110**, 18594–18600 (2006). https://doi.org/10.1021/jp062719k

23. M.K. Petersen, F. Wang, N.P. Blake H. Metiu, G.A. Voth, Excess proton solvation and delocalization in a hydrophilic pocket of the proton conducting polymer membrane Nafion (2005) https://doi.org/10.1021/JP044535G

24. R. Devanathan, A. Venkatnathan, R. Rousseau, M. Dupuis, T. Frigato, W. Gu et al., Atomistic simulation of water percolation and proton hopping in nation fuel cell membrane. J. Phys. Chem. B **114**, 13681–13690 (2010). https://doi.org/10.1021/jp103398b

25. W.Y. Hsu, J.R. Barkley, P. Meakin, Ion percolation and insulator-to-conductor transition in Nafion perfluorosulfonic acid membranes. Macromolecules **13**, 198–200 (1980). https://doi.org/10.1021/ma60073a041

26. G. Gebel, Structural evolution of water swollen perfluorosulfonated ionomers from dry membrane to solution. Polymer (Guildf) **41**, 5829–5838 (2000). https://doi.org/10.1016/S0032-3861(99)00770-3

27. K.A. Mauritz, R.B. Moore, State of understanding of Nafion. Chem. Rev. **104**, 4535–4585 (2004). https://doi.org/10.1021/cr0207123

28. T.D. Gierke, G.E. Munn, F.C. Wilson, The morphology in nafion perfluorinated membrane products, as determined by wide- and small-angle x-ray studies. J. Polym. Sci. Polym. Phys. Ed. **19**, 1687–1704 (1981). https://doi.org/10.1002/pol.1981.180191103

29. C.L. Marx, D.F. Caulfield, S.L. Cooper, Morphology of ionomers. Macromolecules **6**, 344–353 (1973). https://doi.org/10.1021/ma60033a007

30. W.J. Macknight, W.P. Taggart, R.S. Stein, A model for the structure of ionomers. J. Polym. Sci. Polym. Symp. **45**, 113–128 (2007). https://doi.org/10.1002/polc.5070450110

31. W.Y. Hsu, T.D. Gierke, Ion transport and clustering in nafion perfluorinated membranes. J. Memb. Sci. **13**, 307–326 (1983). https://doi.org/10.1016/S0376-7388(00)81563-X

32. M. Fujimura, T. Hashimoto, H. Kawai, Small-angle X-ray scattering study of perfluorinated ionomer membranes. 1. Origin of two scattering maxima. Macromolecules 14, 1309–1315 (1981). https://doi.org/10.1021/ma50006a032

33. M. Fujimura, T. Hashimoto, H. Kawai, Small-angle X-ray scattering study of perfluorinated ionomer membranes. 2. Models for ionic scattering maximum. Macromolecules **15**, 136–144 (1982). https://doi.org/10.1021/ma00229a028

34. B. Dreyfus, G. Gebel, P. Aldebert, M. Pineri, M. Escoubes, M. Thomas, Distribution of the «micelles» in hydrated perfluorinated ionomer membranes from SANS experiments. J. Phys. **51**, 1341–1354 (1990). https://doi.org/10.1051/jphys:0199000510120134100

35. M.H. Litt, Reevaluation of Nafion morphology. Am. Chem. Soc. Polym. Prepr. Div. Polym. Chem. **38**, 80–81 (1997)
36. L. Rubatat, A.L. Rollet, G. Gebel, O. Diat, Evidence of elongated polymeric aggregates in Nafion. Macromolecules **35**, 4050–4055 (2002). https://doi.org/10.1021/ma011578b
37. K. Schmidt-Rohr, Q. Chen, Parallel cylindrical water nanochannels in Nafion fuel-cell membranes. Nat. Mater. **7**, 75–83 (2008). https://doi.org/10.1038/nmat2074
38. J.P. Meyers, J.E. Mcgrath, R. Borup, J. Meyers, B. Pivovar, Y.S. Kim et al., Scientific aspects of polymer electrolyte fuel cell durability and degradation. Chem. Rev. **107**, 3904–3951 (2007). https://doi.org/10.1021/cr050182l
39. M. Kumar, S.J. Paddison, Side-chain degradation of perfluorosulfonic acid membranes: An ab-initio study. J. Mater. Res. 27, 1982–1991 (2012). https://doi.org/10.1557/jmr.2012.191
40. X. Glipa, B. Bonnet, B. Mula, D.J. Jones, J. Rozière, Investigation of the conduction properties of phosphoric and sulfuric acid doped polybenzimidazole. J. Mater. Chem. **9**, 3045–3049 (1999). https://doi.org/10.1039/a906060j
41. Q. Li, J.O. Jensen, R.F. Savinell, N.J. Bjerrum, High temperature proton exchange membranes based on polybenzimidazoles for fuel cells. Prog. Polym. Sci. **34**, 449–477 (2009). https://doi.org/10.1016/j.progpolymsci.2008.12.003
42. D. Rodriguez, C. Jegat, O. Trinquet, J. Grondin, J.C. Lassègues, Proton conduction in poly (acrylamide)-acid blends. Solid State Ionics **61**, 195–202 (1993). https://doi.org/10.1016/0167-2738(93)90354-6
43. P. Musto, F.E. Karasz, W.J. MacKnight, Fourier transform infra-red spectroscopy on the thermo-oxidative degradation of polybenzimidazole and of a polybenzimidazole/polyetherimide blend. Polymer **34**, 2934–2945 (1993). https://doi.org/10.1016/0032-3861(93)90618-K
44. R. Bouchet, E. Siebert, Proton conduction in acid doped polybenzimidazole. Solid State Ionics **118**, 287–299 (1999). https://doi.org/10.1016/S0167-2738(98)00466-4
45. Q. Li, R. He, R.W. Berg, H.A. Hjuler, N.J. Bjerrum, Water uptake and acid doping of polybenzimidazoles as electrolyte membranes for fuel cells. Solid State Ionics **168**, 177–185 (2004). https://doi.org/10.1016/j.ssi.2004.02.013
46. C.E. Hughes, S. Haufe, B. Angerstein, R. Kalim, U. Mähr, A. Reiche et al., Probing structure and dynamics in poly[2,2′-(m-phenylene)-5,5′-bibenzimidazole] fuel cells with magic-angle spinning NMR. J. Phys. Chem. B **108**, 13626–13631 (2004). https://doi.org/10.1021/jp047607c
47. A. Noda, M.A.B. Hasan Susan, K. Kudo, S. Mitsushima, K. Hayamizu, M. Watanabe, Brønsted acid-base ionic liquids as proton-conducting nonaqueous electrolytes. J. Phys. Chem. B **107**, 4024–4033 (2003). https://doi.org/10.1021/jp022347p
48. H. Matsuoka, H. Nakamoto, M.A.B.H. Susan, M. Watanabe, Brønsted acid-base and -polybase complexes as electrolytes for fuel cells under non-humidifying conditions. Electrochim. Acta **50**, 4015–4021 (2005). https://doi.org/10.1016/j.electacta.2005.02.038
49. T.L. Greaves, C.J. Drummond, Protic ionic liquids: properties and applications. Chem. Rev. **108**, 206–237 (2008). https://doi.org/10.1021/cr068040u
50. A. Schechter, R.F. Savinell, Imidazole and 1-methyl imidazole in phosphoric acid doped polybenzimidazole, electrolyte for fuel cells. Solid State Ionics **147**, 181–187 (2002)
51. M.A.B.H. Susan, M. Yoo, H. Nakamoto, M. Watanabe, A novel Brønsted acid–base system as anhydrous proton conductors for fuel cell electrolytes. Chem. Lett. **32**, 836–837 (2003). https://doi.org/10.1246/cl.2003.836
52. M.L. Hoarfrost, M. Tyagi, R.A. Segalman, J.A. Reimer, Proton hopping and long-range transport in the protic ionic liquid [Im][TFSI], probed by pulsed-field gradient NMR and Quasi-elastic neutron scattering. J. Phys. Chem. B **116**, 8201–8209 (2012). https://doi.org/10.1021/jp3044237
53. R. Sood, C. Iojoiu, E. Espuche, F. Gouanvé, G. Gebel, H. Mendil-Jakani et al., Proton conducting ionic liquid doped Nafion membranes: nano-structuration, transport properties and water sorption. J. Phys. Chem. C **116**, 24413–24423 (2012). https://doi.org/10.1021/jp306626y

54. V. Di Noto, M. Piga, G.A. Giffin, S. Lavina, E.S. Smotkin, J.Y. Sanchez et al., Influence of anions on proton-conducting membranes based on neutralized nafion 117, triethylammonium methanesulfonate, and triethylammonium perfluorobutanesulfonate. 2. electrical properties. J. Phys. Chem. C 116, 1370–1379 (2012). https://doi.org/10.1021/jp204242q

55. R. Devanathan, A. Venkatnathan, M. Dupuis, Atomistic simulation of nafion membrane: I. Effect of hydration on membrane nanostructure. J. Phys. Chem. B 111, 8069–8079 (2007). https://doi.org/10.1021/jp0726992

56. A. Venkatnathan, R. Devanathan, M. Dupuis, Atomistic simulations of hydrated nafion and temperature effects on hydronium ion mobility. J. Phys. Chem. B 111, 7234–7244 (2007). https://doi.org/10.1021/jp0700276

57. C.K. Knox, G.A. Voth, Probing selected morphological models of hydrated Nafion using large-scale molecular dynamics simulations. J. Phys. Chem. B 114, 3205–3218 (2010). https://doi.org/10.1021/jp9112409

58. K.A. Mauritz, A.J. Hopfinger, Structural properties of membrane ionomers, in *Modern Aspects of Electrochemistry* (Springer US, Boston, MA, 1982), p. 425–508. https://doi.org/10.1007/978-1-4615-7458-3_6

59. H.L. Yeager, A. Steck, Cation and water diffusion in Nafion Ion exchange membranes: influence of polymer structure. J. Electrochem. Soc. 128, 1880 (1981). https://doi.org/10.1149/1.2127757

60. S.C. Yeo, A. Eisenberg, Physical properties and supermolecular structure of perfluorinated ion-containing (nafion) polymers. J. Appl. Polym. Sci. 21, 875–898 (1977). https://doi.org/10.1002/app.1977.070210401

61. J.A. Elliott, S. Hanna, A.M.S. Elliott, G.E. Cooley, Atomistic simulation and molecular dynamics of model systems for perfluorinated ionomer membranes. Phys. Chem. Chem. Phys. 1, 4855–4863 (1999). https://doi.org/10.1039/a905267d

62. A. Vishnyakov, A.V. Neimark, Molecular simulation study of Nafion membrane solvation in water and methanol. J. Phys. Chem. B 104, 4471–4478 (2000). https://doi.org/10.1021/JP993625W

63. S.S. Jang, V. Molinero, C. Tahir, W.A. Goddard III., Nanophase-segregation and transport in Nafion 117 from molecular dynamics simulations: effect of monomeric sequence. J. Phys. Chem. B 108, 3149–3157 (2004). https://doi.org/10.1021/jp036842c

64. S.S. Jang, V. Molinero, T. Çagin, W.A. Goddard, Effect of monomeric sequence on nanostructure and water dynamics in Nafion 117. Solid State Ionics 175, 805–808 (2004). https://doi.org/10.1016/J.SSI.2004.08.039

65. S. Sengupta, R. Pant, P. Komarov, A. Venkatnathan, A.V. Lyulin, Atomistic simulation study of the hydrated structure and transport dynamics of a novel multi acid side chain polyelectrolyte membrane. Int. J. Hydrogen Energy (2017). https://doi.org/10.1016/j.ijhydene.2017.09.078

66. S. Sengupta, A.V. Lyulin, Molecular dynamics simulations of substrate hydrophilicity and confinement effects in Capped Nafion films. J. Phys. Chem. B 122, 6107–6119 (2018). https://doi.org/10.1021/acs.jpcb.8b03257

67. G. Kritikos, R. Pant, S. Sengupta, K.K. Karatasos, A. Venkatnathan, A.V. Lyulin, Nanostructure and dynamics of humidified Nafion-graphene oxide composites via molecular dynamics simulations. J. Phys. Chem. C 122, 22864–22875 (2018). https://doi.org/10.1021/acs.jpcc.8b07170

68. S. Sengupta, A.V. Lyulin, Molecular modeling of structure and dynamics of Nafion protonation states. J. Phys. Chem. B 123, 6882–6891 (2019). https://doi.org/10.1021/acs.jpcb.9b04534

69. S.J. Paddison, T.A. Zawodzinski Jr., Molecular modeling of the pendant chain in Nafion®. Solid State Ionics 113–115, 333–340 (1998). https://doi.org/10.1016/S0167-2738(98)00298-7

70. S.J. Paddison, L.R. Pratt, T.A. Zawodzinski, Conformations of perfluoroether sulfonic acid side chains for the modeling of Nafion. J. New Mater. Electrochem. Syst. 2, 183–188 (1999)

71. S.J. Paddison, The modeling of molecular structure and ion transport in sulfonic acid based ionomer membranes. J. New Mater. Electrochem. Syst. 4, 197–207 (2001)

72. D.A. Mologin, P.G. Khalatur, A.R. Khokhlov, Structural organization of water-containing Nafion: a cellular-automaton-based simulation. Macromol. Theory Simul. **11**, 587 (2002). https://doi.org/10.1002/1521-3919(20020601)11:5%3c587::AID-MATS587%3e3.0.CO;2-P

73. P.G. Khalatur, S.K. Talitskikh, A.R. Khokhlov, Structural organization of water-containing Nafion: the integral equation theory. Macromol. Theory Simul. **11**, 566 (2002). https://doi.org/10.1002/1521-3919(20020601)11:5%3c566::AID-MATS566%3e3.0.CO;2-0

74. S. Yamamoto, S.A. Hyodo, A computer simulation study of the mesoscopic structure of the polyelectrolyte membrane Nafion. Polym. J. **35**, 519–527 (2003). https://doi.org/10.1295/polymj.35.519

75. P.V. Komarov, I.N. Veselov, P.G. Khalatur, Self-organization of amphiphilic block copolymers in the presence of water: A mesoscale simulation. Chem. Phys. Lett. **605–606**, 22–27 (2014). https://doi.org/10.1016/J.CPLETT.2014.05.004

76. J.T. Wescott, Y. Qi, L. Subramanian, C.T. Weston, Mesoscale simulation of morphology in hydrated perfluorosulfonic acid membranes. J. Chem. Phys. **124**, 134702 (2006). https://doi.org/10.1063/1.2177649

77. P.V. Komarov, I.N. Veselov, P.P. Chu, P.G. Khalatur, Mesoscale simulation of polymer electrolyte membranes based on sulfonated poly (ether ether ketone) and Nafion. Soft Matter **6**, 3939 (2010). https://doi.org/10.1039/b921369d

78. B. Muriithi, D. Loy, Proton conductivity of Nafion/ex-situ sulfonic acid-modified Stöber silica nanocomposite membranes as a function of temperature, silica particles size and surface modification. Membranes (Basel) **6**, 12 (2016). https://doi.org/10.3390/membranes6010012

79. R. Gosalawit, S. Chirachanchai, S. Shishatskiy, S.P. Nunes, Krytox–Montmorillonite–Nafion® nanocomposite membrane for effective methanol crossover reduction in DMFCs. Solid State Ionics **178**, 1627–1635 (2007). https://doi.org/10.1016/J.SSI.2007.10.008

80. M.M. Hasani-Sadrabadi, E. Dashtimoghadam, F.S. Majedi, S. Wu, A. Bertsch, H. Moaddel et al., Nafion/Chitosan-wrapped CNT nanocomposite membrane for high-performance direct methanol fuel cells. RSC Adv. **3**, 7337 (2013). https://doi.org/10.1039/c3ra40480c

81. B.R. Matos, R.A. Isidoro, E.I. Santiago, F.C. Fonseca, Performance enhancement of direct ethanol fuel cell using Nafion composites with high volume fraction of titania. J. Power Sources **268**, 706–711 (2014). https://doi.org/10.1016/J.JPOWSOUR.2014.06.097

82. A.Z. Weber, A. Kusoglu, Unexplained transport resistances for low-loaded fuel-cell catalyst layers. J. Mater. Chem. A **2**, 17207–17211 (2014). https://doi.org/10.1039/C4TA02952F

83. M.A. Modestino, D.K. Paul, S. Dishari, S.A. Petrina, F.I. Allen, M.A. Hickner et al., Self-assembly and transport limitations in confined Nafion films. Macromolecules **46**, 867–873 (2013). https://doi.org/10.1021/ma301999a

84. E. Passalacqua, F. Lufrano, G. Squadrito, A. Patti, L. Giorgi, Nafion content in the catalyst layer of polymer electrolyte fuel cells: effects on structure and performance. Electrochim. Acta **46**, 799–805 (2001). https://doi.org/10.1016/S0013-4686(00)00679-4

85. D. Damasceno Borges, A.A. Franco, K. Malek, G. Gebel, S. Mossa, Inhomogeneous transport in model hydrated polymer electrolyte supported ultrathin films. ACS Nano **7**, 6767–6773 (2013). https://doi.org/10.1021/nn401624p

86. D. Damasceno Borges, G. Gebel, A.A. Franco, K. Malek, S. Mossa, Morphology of supported polymer electrolyte ultrathin films: a numerical study. J. Phys. Chem. C **119**, 1201–1216 (2015). https://doi.org/10.1021/jp507598h

87. F.F. Abraham, Y. Singh, The structure of a hard-sphere fluid in contact with a soft repulsive wall. J. Chem. Phys. **67**, 2384 (1977). https://doi.org/10.1063/1.435080

88. Cha S-H. Recent development of nanocomposite membranes for vanadium redox flow batteries. J. Nanomater. **2015**, 1–12 (2015). https://doi.org/10.1155/2015/207525

89. A. Kusoglu, T.J. Dursch, A.Z. Weber, Nanostructure/swelling relationships of bulk and thin-film PFSA ionomers. Adv. Funct. Mater. **26**, 4961–4975 (2016). https://doi.org/10.1002/adfm.201600861

90. M. Bass, A. Berman, A. Singh, O. Konovalov, V. Freger, Surface-induced Micelle orientation in Nafion films. Macromolecules **44**, 2893–2899 (2011). https://doi.org/10.1021/ma102361f

91. S. Cui, J. Liu, M.E. Selvan, D.J. Keffer, B.J. Edwards, W.V. Steele, A molecular dynamics study of a nafion polyelectrolyte membrane and the aqueous phase structure for proton transport. J. Phys. Chem. B **111**, 2208–2218 (2007). https://doi.org/10.1021/jp066388n

92. M. Tripathy, P.B.S. Kumar, A.P. Deshpande, Molecular structuring and percolation transition in hydrated sulfonated poly (ether ether ketone) membranes. J. Phys. Chem. B **121**, 4873–4884 (2017). https://doi.org/10.1021/acs.jpcb.7b01045

93. T.A. Zawodzinski, C. Derouin, S. Radzinski, R.J. Sherman, V.T. Smith, T.E. Springer et al., Water uptake by and transport through Nafion® 117 membranes. J. Electrochem. Soc. **140**, 1041 (1993). https://doi.org/10.1149/1.2056194

94. M. Bass, A. Berman, A. Singh, O. Konovalov, V. Freger, Surface structure of nafion in vapor and liquid. J. Phys. Chem. B **114**, 3784–3790 (2010). https://doi.org/10.1021/jp9113128

95. S. Goswami, S. Klaus, J. Benziger, Wetting and absorption of water drops on nafion films. Langmuir **24**, 8627–8633 (2008). https://doi.org/10.1021/la800799a

96. N.J. Economou, A.M. Barnes, A.J. Wheat, M.S. Schaberg, S.J. Hamrock, S.K. Buratto, Investigation of humidity dependent surface morphology and proton conduction in multi-acid side chain membranes by conductive probe atomic force microscopy. J. Phys. Chem. B **119**, 14280–14287 (2015). https://doi.org/10.1021/acs.jpcb.5b07255

97. H. Noguchi, K. Taneda, H. Minowa, H. Naohara, K. Uosaki, Humidity-dependent structure of surface water on perfluorosulfonated ionomer thin film studied by sum frequency generation spectroscopy. J. Phys. Chem. C **114**, 3958–3961 (2010). https://doi.org/10.1021/jp907194k

98. O. Kwon, Y. Kang, S. Wu, D.M. Zhu, Characteristics of microscopic proton current flow distributions in fresh and aged nafion membranes. J/ Phys/ Chem/ B **114**, 5365–5370 (2010). https://doi.org/10.1021/jp911182q

99. R.S. McLean, M. Doyle, B.B. Sauer, High-resolution imaging of ionic domains and crystal morphology in ionomers using AFM techniques. Macromolecules **33**, 6541–6550 (2000). https://doi.org/10.1021/ma000464h

100. D. Novitski, S. Holdcroft, Determination of O_2 mass transport at the Pt | PFSA ionomer interface under reduced relative humidity. ACS Appl Mater. Interfaces **7**, 27314–27323 (2015). https://doi.org/10.1021/acsami.5b08720

101. J. Tang, W. Yuan, J. Zhang, H. Li, Y. Zhang, Evidence for a crystallite-rich skin on perfluorosulfonate ionomer membranes. RSC Adv. **3**, 8947–8952 (2013). https://doi.org/10.1039/c3ra40430g

102. F.N. Büchi, S. Srinivasa, Operating proton exchange membrane fuel cells without external humidification of the reactant gases. J. Electrochem. Soc. **144**, 2767 (1997). https://doi.org/10.1149/1.1837893

103. H.S. Park, Y.J. Kim, W.H. Hong, Y.S. Choi, H.K. Lee, Influence of morphology on the transport properties of perfluorosulfonate ionomers/polypyrrole composite membrane. Macromolecules **38**, 2289–2295 (2005). https://doi.org/10.1021/ma047650y

104. K. Pourzare, Y. Mansourpanah, S. Farhadi, Advanced nanocomposite membranes for fuel cell applications: a comprehensive review. Biofuel Res. J. **3**, 496–513 (2016). https://doi.org/10.18331/BRJ2016.3.4.4

105. A. Enotiadis, K. Angjeli, N. Baldino, I. Nicotera, D. Gournis, Graphene-based nafion nanocomposite membranes: enhanced proton transport and water retention by novel organo-functionalized graphene oxide nanosheets. Small **8**, 3338–3349 (2012). https://doi.org/10.1002/smll.201200609

106. G. Liu, W. Jin, N. Xu, Graphene-based membranes. Chem. Soc. Rev. **44**, 5016–5030 (2015). https://doi.org/10.1039/c4cs00423j

107. B.G. Choi, Y.S. Huh, Y.C. Park, D.H. Jung, W.H. Hong, H. Park, Enhanced transport properties in polymer electrolyte composite membranes with graphene oxide sheets. Carbon N Y **50**, 5395–5402 (2012). https://doi.org/10.1016/j.carbon.2012.07.025

108. R. Kumar, C. Xu, K. Scott, Graphite oxide/Nafion composite membranes for polymer electrolyte fuel cells. RSC Adv. **2**, 8777 (2012). https://doi.org/10.1039/c2ra20225e

109. H. Zarrin, D. Higgins, Y. Jun, Z. Chen, M. Fowler, Functionalized graphene oxide nanocomposite membrane for low humidity and high temperature proton exchange membrane fuel cells. J. Phys. Chem. C **115**, 20774–20781 (2011). https://doi.org/10.1021/jp204610j

110. D.C. Lee, H.N. Yang, S.H. Park, W.J. Kim, Nafion/graphene oxide composite membranes for low humidifying polymer electrolyte membrane fuel cell. J. Memb. Sci. **452**, 20–28 (2014). https://doi.org/10.1016/j.memsci.2013.10.018
111. M.R. Karim, K. Hatakeyama, T. Matsui, H. Takehira, T. Taniguchi, M. Koinuma et al., Graphene oxide nanosheet with high proton conductivity. J. Am. Chem. Soc. **135**, 8097–8100 (2013). https://doi.org/10.1021/ja401060q
112. T. Bayer, S.R. Bishop, M. Nishihara, K. Sasaki, S.M. Lyth, Characterization of a graphene oxide membrane fuel cell. J. Power Sources **272**, 239–247 (2014). https://doi.org/10.1016/j.jpowsour.2014.08.071
113. L. Wang, J. Kang, J.-D. Nam, J. Suhr, A.K. Prasad, S.G. Advani, Composite membrane based on graphene oxide sheets and Nafion for polymer electrolyte membrane fuel cells. ECS Electrochem. Lett. **4**, F1-4 (2014). https://doi.org/10.1149/2.0021501eel
114. Z. Jiang, X. Zhao, Y. Fu, A. Manthiram, Composite membranes based on sulfonated poly(ether ether ketone) and SDBS-adsorbed graphene oxide for direct methanol fuel cells. J. Mater. Chem. **22**, 24862–24869 (2012). https://doi.org/10.1039/c2jm35571j
115. N. Üregen, K. Pehlivanoğlu, Y. Özdemir, Y. Devrim, Development of polybenzimidazole/graphene oxide composite membranes for high temperature PEM fuel cells. Int. J. Hydrog. Energ **42**, 2636–2647 (2017). https://doi.org/10.1016/j.ijhydene.2016.07.009
116. R. Rudra, V. Kumar, N. Pramanik, P.P. Kundu, Graphite oxide incorporated crosslinked polyvinyl alcohol and sulfonated styrene nanocomposite membrane as separating barrier in single chambered microbial fuel cell. J. Power Sources **341**, 285–293 (2017). https://doi.org/10.1016/j.jpowsour.2016.12.028
117. K. Karatasos, G. Kritikos, Characterization of a graphene oxide/poly(acrylic acid) nanocomposite by means of molecular dynamics simulations. RSC Adv. **6**, 109267–109277 (2016). https://doi.org/10.1039/C6RA22951D
118. K. Karatasos, G. Kritikos, A microscopic view of graphene-oxide/poly(acrylic acid) physical hydrogels: effects of polymer charge and graphene oxide loading. Soft Matter **14**, 614–627 (2018). https://doi.org/10.1039/c7sm02305g
119. R. Devanathan, D. Chase-Woods, Y. Shin, D.W. Gotthold, Molecular dynamics simulations reveal that water diffusion between graphene oxide layers is slow. Sci. Rep. **6**, 1–8 (2016). https://doi.org/10.1038/srep29484
120. S. Feng, G.A. Voth, Proton solvation and transport in hydrated nafion. J. Phys. Chem. B **115**, 5903–5912 (2011). https://doi.org/10.1021/jp2002194
121. R. Devanathan, A. Venkatnathan, R. Rousseau, M. Dupuis, T. Frigato, W. Gu et al., Atomistic simulation of water percolation and proton hopping in Nafion fuel cell membrane. J. Phys. Chem. B **114**, 13681–13690 (2010). https://doi.org/10.1021/jp103398b
122. M. Ester, H.-P. Kriegel, J. Sander, X. Xu, A density-based algorithm for discovering clusters in large spatial databases with noise, in *KDD-96 Proceedings*, vol. 96, p. 226–231 (1996). https://doi.org/10.1103/physicsphysiquefizika.3.255
123. M.E. Fisher, The theory of condensation and the critical point. Phys. Phys. Fiz **3**, 255–283 (1967). https://doi.org/10.1103/PhysicsPhysiqueFizika.3.255
124. W. vanMegen, T.C. Mortensen, J. Müller, S.R. Williams, W. van Megen, T.C. Mortensen et al., Measurement of the self intermediate scattering function of suspensions of hard spherical particles near the glass transition. Phys. Rev. E **58**, 6073–6085 (1998). https://doi.org/10.1103/PhysRevE.58.6073
125. R. Kohlrausch, Theorie des elektrischen Rückstandes in der Leidener Flasche. Ann. Phys. **167**, 179–214 (1854). https://doi.org/10.1002/andp.18541670203
126. K.L. Ngai, *Relaxation and Diffusion in Complex Systems* (Springer, New York, 2011) https://doi.org/10.1007/978-1-4419-7649-9
127. G. Kritikos, K. Karatasos, Temperature dependence of dynamic and mechanical properties in poly(acrylic acid)/graphene oxide nanocomposites. Mater. Today Commun. **13**, 359–366 (2017). https://doi.org/10.1016/j.mtcomm.2017.11.006
128. G. Kritikos, N. Vergadou, I.G. Economou, Molecular dynamics simulation of highly confined Glassy ionic liquids. J. Phys. Chem. C **120**, 1013–1024 (2016). https://doi.org/10.1021/acs.jpcc.5b09947

129. R. Devanathan, A. Venkatnathan, M. Dupuis, Atomistic simulation of Nafion membrane. 2. Dynamics of water molecules and hydronium ions. J. Phys. Chem. B111, 13006–13013 (2007). https://doi.org/10.1021/jp0761057

130. S. Pahari, C.K. Choudhury, P.R. Pandey, M. More, A. Venkatnathan, S. Roy, Molecular dynamics simulation of phosphoric acid doped monomer of polybenzimidazole: a potential component polymer electrolyte membrane of fuel cell. J. Phys. Chem. B **116**, 7357–7366 (2012). https://doi.org/10.1021/jp301117m

131. S. Pahari, S. Roy, Structural and conformational properties of polybenzimidazoles in melt and phosphoric acid solution: a polyelectrolyte membrane for fuel cells. RSC Adv. **6**, 8211–8221 (2016). https://doi.org/10.1039/C5RA22159E

132. K. Shirata, S. Kawauchi, Effect of benzimidazole configuration in polybenzimidazole chain on interaction with phosphoric acid: a DFT study. J. Phys. Chem. B **119**, 592–603 (2015). https://doi.org/10.1021/jp510067n

133. S.C. Kumbharkar, U.K. Kharul, New N-substituted ABPBI: synthesis and evaluation of gas permeation properties. J. Memb. Sci. **360**, 418–425 (2010). https://doi.org/10.1016/j.memsci.2010.05.041

134. M.A. Habib, J.O. Bockris, Adsorption at the solid/solution interface. An FTIR study of phosphoric acid on platinum and gold. J. Electrochem. Soc.132, 108 (1985)

135. M. Kumar, A. Venkatnathan, Mechanism of proton transport in ionic-liquid-doped perfluorosulfonic acid membranes. J. Phys. Chem. B **117**, 14449–14456 (2013). https://doi.org/10.1021/jp408352w

136. M. Kumar, A. Venkatnathan, Quantum chemistry study of proton transport in imidazole chains. J. Phys. Chem. B **119**, 3213–3222 (2015). https://doi.org/10.1021/jp508994c

137. R. Pant, M. Kumar, A. Venkatnathan, Quantum mechanical investigation of proton transport in imidazolium methanesulfonate ionic liquid. J. Phys. Chem. C **121**, 7069–7080 (2017). https://doi.org/10.1021/acs.jpcc.6b11997

138. A.P. Sunda, M. More, A. Venkatnathan, A molecular investigation of the nanostructure and dynamics of phosphoric-triflic acid blends of hydrated ABPBI [poly(2,5-benzimidazole)] polymer electrolyte membranes. Soft Matter **9**, 1122–1132 (2013). https://doi.org/10.1039/c2sm26927a

139. M. More, S. Pahari, S. Roy, A. Venkatnathan, Characterization of the structures and dynamics of phosphoric acid doped benzimidazole mixtures: a molecular dynamics study. J. Mol. Model **19**, 109–118 (2013). https://doi.org/10.1007/s00894-012-1519-8

140. M. More, A.P. Sunda, A. Venkatnathan, Polymer chain length, phosphoric acid doping and temperature dependence on structure and dynamics of an ABPBI [poly(2,5-benzimidazole)] polymer electrolyte membrane. RSC Adv. **4**, 19746–19755 (2014). https://doi.org/10.1039/c4ra01421a

141. J.G.E.M. Fraaije, B.A.C. van Vlimmeren, N.M. Maurits, M. Postma, O.A. Evers, C. Hoffmann et al., The dynamic mean-field density functional method and its application to the mesoscopic dynamics of quenched block copolymer melts. J. Chem. Phys. **106**, 4260–4269 (1997). https://doi.org/10.1063/1.473129

142. P.J. Hoogerbrugge, J.M.V.A. Koelman, Simulating microscopic hydrodynamic phenomena with dissipative particle dynamics. Europhys. Lett. **19**, 155–160 (1992). https://doi.org/10.1209/0295-5075/19/3/001

143. N.M. Maurits, B.A.C. Van Vlimmeren, J.G.E.M. Fraaije, Mesoscopic phase separation dynamics of compressible copolymer melts. (1997)

144. N.M. Maurits, A.V.M. Zvelindovsky, G.J.A. Sevink, B.A.C. Van Vlimmeren, J.G.E.M. Fraaije, N.M. Maurits et al., Hydrodynamic effects in three-dimensional microphase separation of block copolymers). Hydrodynamic effects in three-dimensional microphase separation of block copolymers: Dynamic mean-field density functional approach. J. Chem. Phys. **108**, 9150–9154 (1998). https://doi.org/10.1063/1.476362.

145. A.V.M. Zvelindovsky, G.J.A. Sevink, B.A.C. van Vlimmeren, N. Maurits, J.E.M. Fraaije, Three-dimensional mesoscale dynamics of block copolymers under shear: The dynamic density-functional approach: the dynamic density-functional approach. Phys. Rev. E **57**, R4879–R4882 (1998)

146. J.J. Krueger, P.P. Simon, H.J. Ploehn, Phase behavior and microdomain structure in perfluo-rosulfonated ionomers via self-consistent mean field theory (2002). https://doi.org/10.1021/MA0020638

147. J.M.V.A. Koelman, P.J. Hoogerbrugge, Dynamic simulations of hard-sphere suspensions under steady shear. Europhys. Lett. **21**, 363–368 (1993). https://doi.org/10.1209/0295-5075/21/3/018

148. R.D. Groot, P.B. Warren, Dissipative particle dynamics: bridging the gap between atomistic and mesoscopic simulation. J. Chem. Phys. **107**, 4423–4435 (1997). https://doi.org/10.1063/1.474784

149. P.J. Flory, M. Volkenstein, Statistical mechanics of chain molecules. Biopolymers **8**, 699–700 (1969). https://doi.org/10.1002/bip.1969.360080514

150. J. Bicerano, *Prediction of Polymer Properties* (Marcel Dekker, 2002)

151. M.L. Huggins, The solubility of nonelectrolytes. By Joel H. Hildebrand and Robert S. Scott. J. Phys. Chem. **55**, 619–620 (1951). https://doi.org/10.1021/j150487a027.

152. P.J. Flory, Fifteenth Spiers Memorial Lecture. Thermodynamics of polymer solutions. Discuss. Faraday Soc. 49, 7 (1970). https://doi.org/10.1039/df9704900007

153. A.A. Askadiskii, V.I. Kondraschenko, Computer material science of polymers. Sci. World **1**, 544 (1999)

154. R. Consiglio, D.R. Baker, G. Paul, H.E. Stanley, Continuum percolation thresholds for mixtures of spheres of different sizes. Phys. A Stat. Mech. Its Appl. **319**, 49–55 (2003). https://doi.org/10.1016/S0378-4371(02)01501-7

155. M.J. Park, K.H. Downing, A. Jackson, E.D. Gomez, A.M. Minor, D. Cookson et al., Increased water retention in polymer electrolyte membranes at elevated temperatures assisted by capillary condensation (2007). https://doi.org/10.1021/NL072617L

156. S. Förster, M. Konrad, From self-organizing polymers to nano- and biomaterials. J. Mater. Chem. **13**, 2671–2688 (2003). https://doi.org/10.1039/B307512P